Mechanical Engineering

Proceedings of the 6th Baltic Mechatronics Symposium

Tallinn April 27, 2021

Kiviluoma Panu
Kuosmanen Petri
Otto Tauno

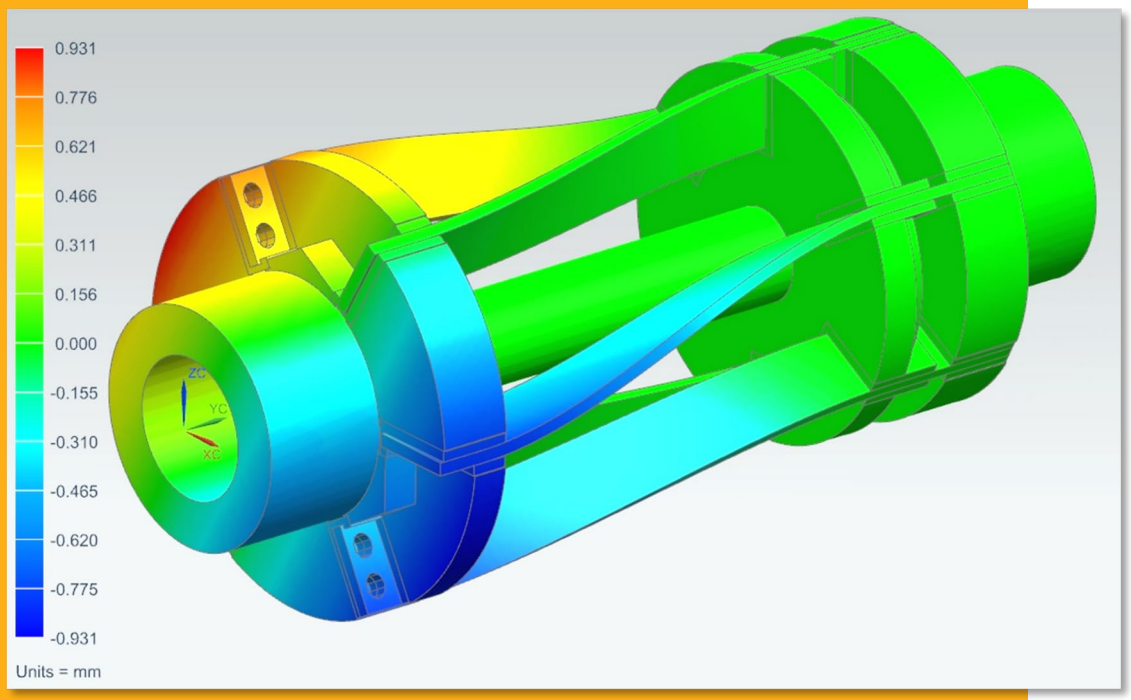

Aalto University
School of Engineering

TAL TECH

Proceedings of the 6th Baltic Mechatronics Symposium

Tallinn April 27, 2021

Kiviluoma Panu
Kuosmanen Petri
Otto Tauno

Aalto University
School of Engineering
Mechanical Engineering

Tallinn University of Technology
School of Engineering
Department of Mechanical and Industrial Engineering

Cover image by Kalle Kinnunen, Alvari Seppänen and Tommaso Turrin (Project Coupler)
ISBN 978-952-64-9605-4 (pdf)

Abstract

Aalto University, P.O. Box 11000, FI-00076 Aalto www.aalto.fi
TALTECH, Ehitajate tee 5, 19086 Tallinn, Estonia www.ttu.ee

Author
Kiviluoma Panu, Kuosmanen Petri, Otto Tauno

Name of the publication
Proceedings of the 6th Baltic Mechatronics Symposium
Publisher Aalto University School of Engineering
Unit Mechanical Engineering
Field of research Mechanical Engineering
Language English

Abstract

The Baltic Mechatronics Symposium is annual symposium with the objective to provide a forum for young scientists from Baltic countries to exchange knowledge, experience, results and information in large variety of fields in mechatronics. This year the Symposium was organized alongside the Modern Materials and Manufacturing 2021 Conference in Tallinn in co-operation with Taltech and Aalto University. Due to the ongoing COVID-19 situation the symposium was organized as a virtual meeting.

The content of the proceedings

1. Accurate Dispensing of Liquids with Various Viscosities
2. Coupling with Adjustable Stiffness
3. Elasto-Magnetic Load Measurement
4. Effects of Pressure and Air Flow on Drying Rate of Nano Paper
5. Ultra-Wideband Localization for Crane-Robot Cooperation
6. Improving Tunnel Mode Efficiency of Combined Azimuth Thruster

Keywords Mechatronics, Industrial Internet, Sensors, Actuators, Control
ISBN (pdf) 978-952-64-9605-4
Location of publisher Helsinki
Pages 37

Accurate Dispensing of Liquids with Various Viscosities

Alexander Björklund[1*, a], Joonas Sipiläinen[2,b] and Joel Stening[2,c]

Panu Kiviluoma[2,d], Petri Kuosmanen[2,e],

[1]Department of Electrical Engineering and Automation, Aalto University, Finland

[2]Department of Mechanical Engineering, Aalto University, Finland

[A]alexander.bjorklund@aalto.fi, [b]joonas.sipilainen@aalto.fi, [c]joel.stening@aalto.fi, [d]panu.kiviluoma@aalto.fi, [e]petri.kuosmanen@aalto.fi

Keywords: peristaltic pump, flow measurement, load cell, Arduino

Abstract

Accurate dispensing methods reduces waste of products and ensures that the promised amount of a product is delivered. The accuracy of a flow meter, weight measurement of a container and time-based measurement is tested by pumping 100 g, 200 g and 300 g of liquid through a peristaltic pump and analyzing the deviations in mass from the desired amount. The fluids used for testing are liquid soap, water, conditioner, and hand sanitizer. Based on the results, it is concluded that weight measurement is the most accurate, and that the viscosity and chemical structure of the liquid affects the accuracy of the dispensing methods.

Introduction

Fluid dispensing technology can be described as a controlled and accurate distribution process for fluids [1]. Different dispensers have been applied to various commercial products and industries. Beverages are often dispensed by some sort of dispensing unit in bars and restaurants. Particularly the food industry has been using dispensers for products for a long time. In addition, dispensers for medical use [2] and other industries can be found. During the time of the global Covid-19 pandemic, non-contact dispensing of hand sanitizer has also become more important.

Different technologies and systems can be implemented to control that a device dispenses liquids with a specified accuracy. For example, time-pressure dispensing, auger pump dispensing, piston valve dispensing, and jetting dispensing [3] are used in the field of circuit assembly and chip packaging, where the accuracy of the dispensed fluids are highly important [4,5]. Optic light can also be used as a control method to achieve nanolitre accuracies [6]. These examples are mainly used for micro- and nanofluid dispensing, but this paper will be focusing on accuracy in dispensing liquids in the hundreds of millilitre scale.

The purpose of this study was to investigate control methods for liquid dispensing and examine which method produces high enough accuracies for commercial use, and to compare the accuracy of the methods with liquids of different viscosities. Weight measurement of a container, time measurement and flow measurement were the control methods examined. These methods have been chosen because of their simplicity and potential in producing accurate results for the volumes they are applied on.

Methods

The goal of this study was to determine the most accurate and reliable dispensing method that works with a wide variety of liquids, without the need of knowing exact densities or viscosities. The

tests were focused on common consumer products with differing physical properties and dispensing methods that are practical for consumer product dispensers.

Testing rig was constructed to enable all tests to be conducted with the same rig. The tests required integrated weight sensing of the liquid container and a flow meter integrated into the tubing before target container. To test pumping volume as function of time we simply need the pump that is connected with tubes. The testing rig can be seen in Fig. 1.

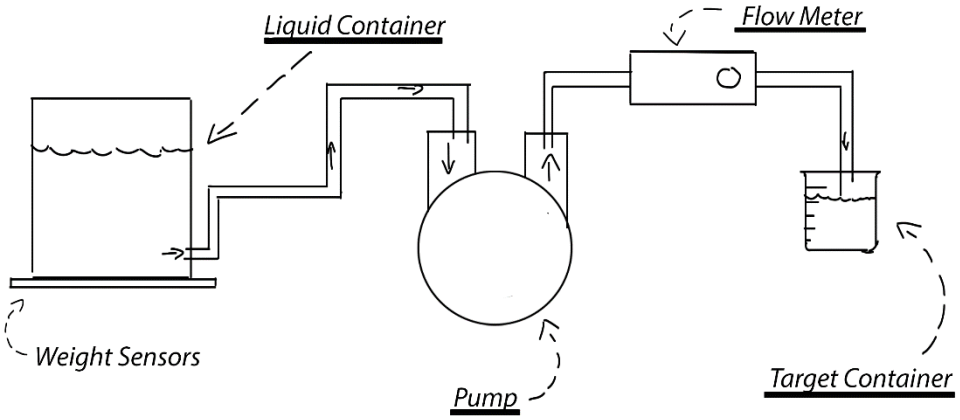

Figure 1. Testing rig and its subsystems. Arrows inside the tubing describe the direction of the flow.

Electronic Components. The dispenser is controlled by an Arduino Uno which allows versatile actuator controls and sensor compatibilities. The liquids are transferred using a peristaltic pump and food grade silicone tubing. Load cell sensors and a flow meter are used for controlling the pump.

The peristaltic pump was chosen for its high accuracy and good hygiene features resulting from its operational principle [7]. The pump has three rollers squishing the silicone tubing running through it, always displacing a certain amount of liquid per revolution which makes dispensing accurate. The easily replaceable silicone tubing is a part of the pumping mechanism and its only product contact surface. By replacing the pump's silicone tubing, all cross contamination between the products can be eliminated when changing dispensed products.

The peristaltic pump has no feedback for the dispensed volumes which is why the dispensing must be controlled in an open loop by timing the pumping time or in a closed loop by measuring the weight of the remaining liquid or by measuring the dispensed volume. In open loop control the timing of the pump is controlled by Arduino and in closed loops by readings from load cell sensors or flow meter. All components of the dispenser are listed in Table 1.

Load cell sensors are used to weigh the remaining liquid in the main container. These sensors were chosen for their accuracy and easy implementation. They are commonly used in consumer scales and have sufficient accuracy for dispensing within the regulation tolerances. Weighing of the main container was chosen since it can be implemented with less sources of error compared to weighing the target container, which will be constantly switched and weighing it would need the scale to be tared before dispensing. The scale features were implemented using Arduino. The system scale was calibrated before dispensing to match the readings of the scale used for reading the test results. After calibration, the readings of the scale fluctuated between two grams above and below the actual weight.

The flow sensor is installed at the outlet of the dispenser to measure the actual dispensed volume. The flow sensor has a resolution of 0.17 ml per pulse which is sufficiently accurate to meet regulation tolerances. The benefit of a flow rate sensor is the assurance of the actual flow rates, but they come at the cost of extra product contact parts which must be cleaned when changing liquids. The resolution of the flow sensor was verified by checking the pulse counts after dispensing 100 ml. This test was repeated four times and the average resolution of these tests was 0.17 ml, however one of the tests resulted in a resolution of 0.14 ml which does not match the manufacturer's specifications. This measurement was dismissed as an outlier.

Table 1. Electronic components of the dispenser.

Component	Specification	Purpose
Controller	Arduino Uno	Control of dispensing
Peristaltic pump	400 mL/min, unbranded	Transfer of liquids
Motor controller	L298N	Control of peristaltic pump
Load cell sensors	0-50 kg	Measuring the weight of remaining liquids
Amplifier	HX711	Amplifying load cell sensor readings
Flow meter	YF-S401, 5880 pulses / liter, 0.17 ml / pulse	Reading of actual dispensed volume
Silicone tubing	9 mm outer diameter, 6 mm inner diameter	Transfer of liquids

Requirements for dispensing accuracy come from consumer packaging regulations set in the EU directive 76/211/EEC. Dispensing accuracy must be within the directives tolerable negative error (TNE). Between 100 ml and 200 ml TNE is 4.5 % of the nominal volume or weight and at 300 ml TNE is 3 % of nominal volume or weight. [8]

Testing. To determine the most accurate dispensing control method, liquids of different viscosities were dispensed in a timing based open-loop control system and weight- and dispensed volume based closed-loop systems. The tested liquids were water, liquid soap, hair conditioner, and hand sanitizer. Each liquid was dispensed at volumes of 100 ml, 200 ml, and 300 ml, as TNE differs with the volumes and the dispensing must be accurate enough at each tolerance level. Three tests were conducted for each target volume for each liquid. The weights of the dispensed liquids were measured with a scale and volumes were calculated based on the densities of the liquids.

Exact viscosities of these liquids were not determined but according to literature, water was ranked least viscous, liquid soap more viscous than water and hair conditioner the most viscous of the tested fluids [9]. Viscosities of hand sanitizers vary between manufacturers and formulations and the viscosity of the tested hand sanitizer could not be ranked based on literature. However, we estimate its viscosity to be between water and liquid soap. Densities of liquid soap, hand sanitizer, and hair conditioner were determined by weighing in a measuring glass and for water's density a literature standard of 1.000 g/ml was used [10]. The density of liquid soap was measured to be 1.0476 g/ml, hand sanitizer 0.8608 g/ml, and hair conditioner 0.8928 g/ml.

Test 1. The liquids were dispensed based on the timing of the pump in an open-loop system. Pumping capacity of the pump was determined by pumping water for 20 seconds and calculating the average pumping capacity. The pump was able to pump 6.84 ml of water per second and dispensing times for different target volumes were calculated based on this.

Test 2. Dispensing accuracy was tested in a closed-loop system by measuring the weight of the remaining liquids in the main container. The remaining liquid was measured with four load cell sensors and the dispensing was cut off when the dispensers load cell sensors detected a loss of weight corresponding to the volume to be dispensed. Densities were not compensated yet as the goal is to dispense as accurately as possible without any information of the dispensed liquid, and 1 g was assumed to correspond to 1 ml.

Test 3. Dispensing accuracy was tested in a closed-loop system, where the pumping was controlled by the measurements of the flow meter. The flow meter was positioned at the outlet of the dispensing system and the pump was stopped once the target volume was reached.

Results

The results of the tests are displayed in Fig. 2 and Table 2. Time-based dispensing was determined to be the most precise dispensing method with the lowest standard deviations for most target volumes and liquids. However, weight based dispensed average volumes reached the TNE requirements more consistently. TNE volumes were 95.5 ml for 100 ml target volume, 191 ml for 200 ml target volume, and 291 ml for 300 ml target volume. Volume based dispensing data is incomplete due to the used flow meter being incapable of properly measuring flows of most of the tested liquids. Therefore, the results of volume-based dispensing will not be further discussed.

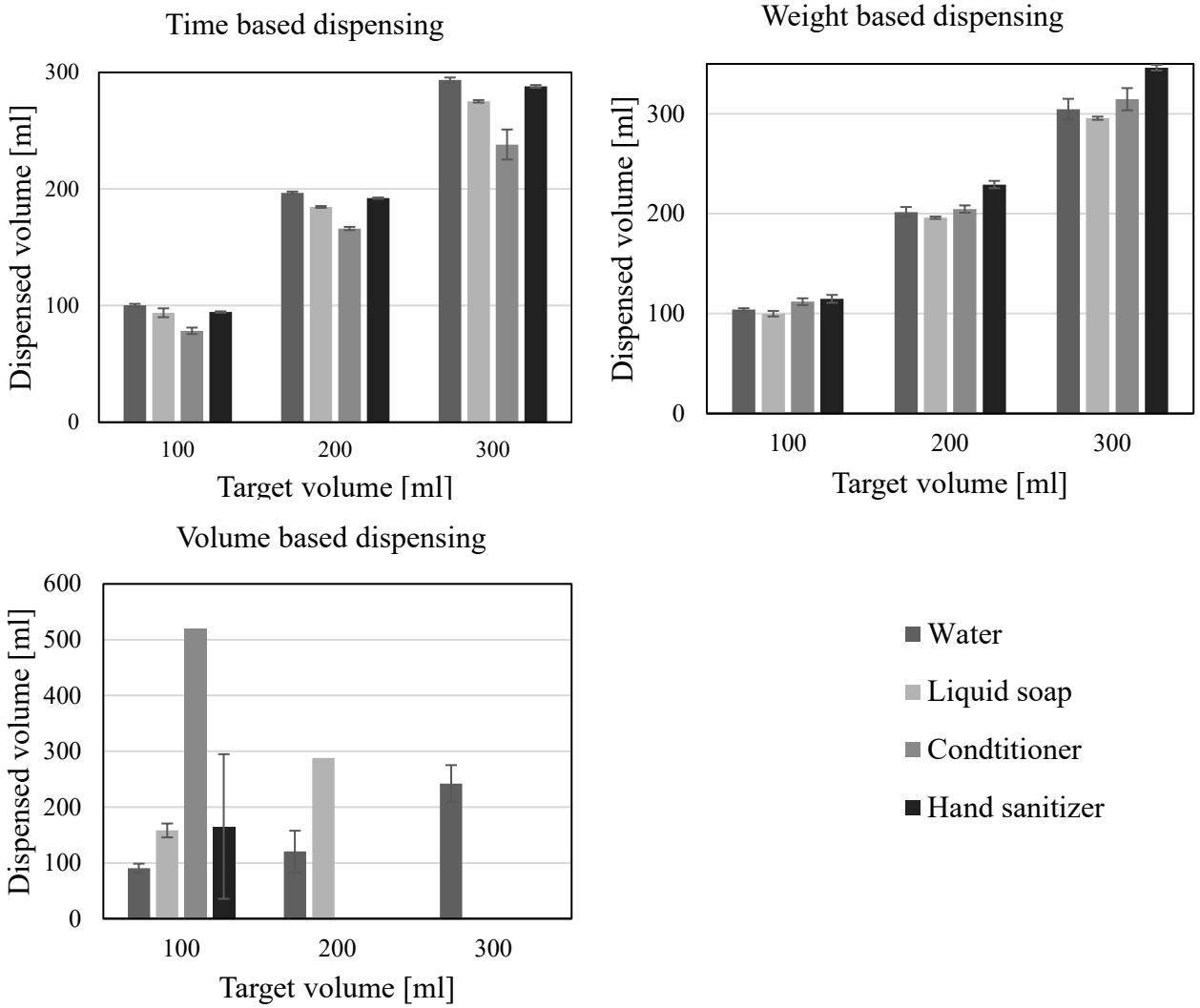

Figure 2. Graphic representation of test results. Calculated average volumes and standard deviations for water, liquid soap, conditioner, and hand sanitizer, dispensed based on time, weight, and volume measurements. Volume measurements are incomplete due to the flow meter being unable to measure certain liquids.

Table 2. Numerical test results with calculated average dispensed volumes and standard deviations.

Dispensing method	Target volume [ml]	Water [ml]		Liquid soap [ml]		Conditioner [ml]		Hand sanitizer [ml]	
		Volume	st.dev	Volume	st.dev	Volume	st.dev	Volume	st.dev
Time	100.0	100.3	1.3	93.9	3.8	78.4	2.8	94.6	0.6
	200.0	196.8	1.1	184.6	0.8	166.2	1.4	192.2	0.6
	300.0	293.5	2.2	275.2	1.1	238.2	12.9	288.0	1.2
Weight	100.0	104.0	1.4	99.9	2.7	111.9	3.4	114.8	3.9
	200.0	201.8	5.0	196.0	1.2	204.7	3.6	229.2	3.7
	300.0	304.7	10.3	295.6	1.6	314.6	11.1	346.2	2.8
Volume	100.0	90.4	8.3	158.1	12.4	519.4	467.1	165.1	129.7
	200.0	120.4	37.3	288.0					
	300.0	242.0	33.1						

Discussion

The time-based dispensing method only produces four results that are within the requirements set by the EU directive 76/211/EEC [8]. Three of these are when the pumped liquid is water. This is due to using the same flow constant of water through the pump of 6.84 ml/s when dispensing all liquids. We can see from the results that the higher viscosity of the liquid, the less amount of liquid is transferred. It can be concluded that the viscosity of the liquids needs to be considered in time-based dispensing with the used TNEs. If the viscosities are considered, the method would probably produce more accurate results than the weight-based dispensing for the tested liquids, since it is more precise.

All produced results are within the TNE when using the weight-based dispensing method. However, overshoots up to 15,4% can be measured. This inaccuracy is probably due to the load cells being inaccurate, causing a creep effect on the results.

The flow meter worked when transferring water, but it did not produce accurate results. When transferring the other liquids, it either stopped measuring the flow completely, or stopped sending pulse information to the system. This is probably due to the flow meter not being compatible with liquids with a higher viscosity than water. The alcohol in the hand sanitizer could also cause damage to the meter if used during a longer period. It can be concluded that a flow meter of higher quality should be used to get accurate results with liquids of different viscosities.

The conditioner has such a high viscosity that there is a risk of an empty space forming at the end of the tubing. When dispensing conditioner or other high-viscosity liquids, this risk should be considered by mixing the liquid frequently whilst dispensing, to avoid inaccurate dispensing results.

More high quality and accurate electronics could be used to achieve more accurate results, but the components used are accurate enough to produce relevant results when comparing to the TNEs in the EU directive 76/211/EEC [8], which producers in the European union need to follow.

If one wants to build a simple measurement system for dispensing liquids without taking into account viscosities, a weight-based control system is the most accurate when comparing the three methods presented in this paper. When dispensing liquids, one usually wants to dispense a certain volume. Therefore, by using a weight-based system, the density of the liquids needs to be known so that it can be implemented in the calculations. Even though an additional parameter needs to be considered using this method, densities of dispensed products are easily measurable compared to the viscosities.

References

[1] Y.X. Zhao, X.D. Chen and X. Chen, *A review of fluid dispensing in microelectronic packaging*, Hydraulic and Pneumatic, vol. 2, pp. 52-54, 2006.

[2] Brolin, A. et al. *Design of automated medicine vending machine using mechatronics techniques*, in IOP conference series. 2018, Materials Science and Engineering. [Online]. 1 August 2018 IOP Publishing. p. 12044–.

[3] X. Cheng, G. Deng, C. Zhou, N. Wang and W. Cui, *Study on the process of fluid Jet dispensing based on high and low voltage drive,* 2017 18th International Conference on Electronic Packaging Technology (ICEPT), Harbin, 2017, pp. 262-265, doi: 10.1109/ICEPT.2017.8046451.

[4] Anoop Raghav S et al., *Design of an automated dispenser unit*, 2014 IEEE International Conference on Electronics, Computing and Communication Technologies (CONECCT), Bangalore, India, 2014, pp. 1-4, doi: 10.1109/CONECCT.2014.6740306.

[5] L. Jianping, D. Guiling, *Technology development and basic theory study of fluid dispensing - a review*, Proceedings of the Sixth IEEE CPMT Conference on High Density Microsystem Design and Packaging and Component Failure Analysis (HDP '04), Shanghai, China, 2004, pp. 198-205, doi: 10.1109/HPD.2004.1346698.

[6] S. Liu, D. Xu, Y. Li, F. Shen and D. Zhang, *Nanoliter Fluid Dispensing Based on Microscopic Vision and Laser Range Sensor*, in IEEE Transactions on Industrial Electronics, vol. 64, no. 2, pp. 1292-1302, Feb. 2017, doi: 10.1109/TIE.2016.2611459.

[7] B. Orchard, *Laboratories and industry provide opportunities for peristaltic pumps*, 2004 World Pumps Volume 2004, Issue 448, pp. 24-26, doi: 10.1016/S0262-1762(04)00063-X

[8] Council Directive 76/211/EEC, *Council Directive of 20 January 1976 on the approximation of the laws of the Member States relating to the making-up by weight or by volume of certain prepackaged products*, 1976, ANNEX I

[9] Process Engineer's Tools, *Viscosity of 150+ common liquid* [Online]. Available: https://powderprocess.net/Tools_html/Data_Diagrams/Chemical_Compound_Liquid_Viscosity.html [Accessed 23- Mar- 2021].

[10] R. Seppänen, L. Mannila, M. Kervinen, I, Parkkila, P. Konttinen, L. Karkela, T. Yli-kokko, *MAOL-taulukot*, 1th ed. Keuruu, Finland, Otavan kirjapaino Oy, 2013.

Coupling with Adjustable Torsional Stiffness

Kalle Kinnunen[1,a], Alvari Seppänen[1,b], Tommaso Turrin[2,c], Risto Viitala[1,d]
Petri Kuosmanen[1,e] and Panu Kiviluoma[1,f]

[1]Department of Mechanical Engineering, Aalto University, Finland

[2]Department of Industrial Engineering, Trento University, Italy

[a]kalle.kinnunen@aalto.fi, [b]alvari.seppanen@aalto.fi, [c]tommaso.turrin@aalto.fi,
[d]risto.viitala@aalto.fi, [e]petri.kuosmanen@aalto.fi, [f]panu.kiviluoma@aalto.fi

Keywords: Powertrain, torsional vibrations, resonance

Abstract

Power generation and industrial operations apply widely machinery with rotating powertrains. The powertrain may suffer from torsional vibrations if the frequency of periodically applied excitation is equal or close to natural frequency of the system. In this research a coupling with adjustable torsional stiffness was developed. With the developed coupling the torsional resonance frequency of the system could be adjusted in the range of 17 to 46 Hz.

Introduction

Resonance occurs when the frequency of periodically applied excitation is equal or close to natural frequency of the system. Vibrations caused by resonance effect are more commonly experienced with larger machines, such as paper machines and large generators [1].

A coupling is a device used to mechanically connect two shafts in order to transmit torque (Fig. 1). The coupling stiffness must be high enough to allow efficient torque transmission, but also the device has to be able to operate under conditions like misalignment which require flexibility. The torsional stiffness of the coupling affects the natural frequencies of the powertrain and it needs to be considered when selecting a coupling.

Typically, the torsional stiffness of the couplings is not adjustable and only few commercial solutions exist. They require disassembly of coupling and changing of parts to adjust the stiffness [2]. Various prototypes of coupling with adjustable torsional stiffness have been made and tested during research in other universities [3,4]. The goal of this research was to determine the torsional stiffness range of a new coupling design, which has easily adjustable torsional stiffness. The torsional stiffness was determined by using analytical calculations, FEM simulation and practical measurements. Also, torsional vibration tests were made to study if the coupling has the capability to adjust the torsional natural frequencies of a rotating shaft line.

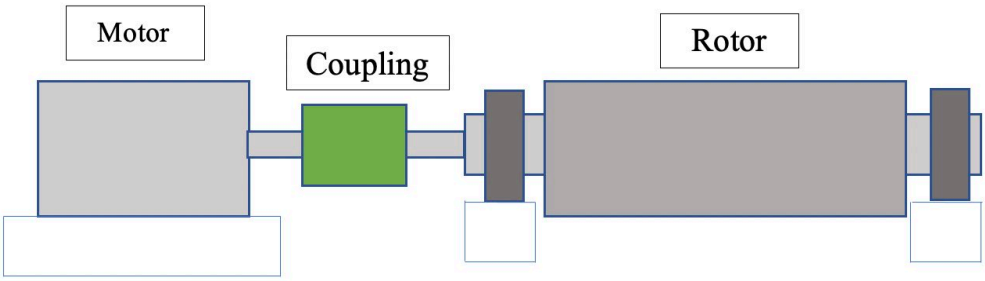

Figure 1. Typical motor-rotor coupling connection.

Methods

Torsional vibration. Torsional vibration is an oscillation of axial rotation between two points in rotating shaft or machine element (Fig. 2). The vibrations typically manifest when transmitting power, for example in gearboxes or crankshafts. The vibration is excited when periodic torque is applied to a shaft and the shaft twists in radial direction, creating a phase difference in angular displacement between the shaft ends [5].

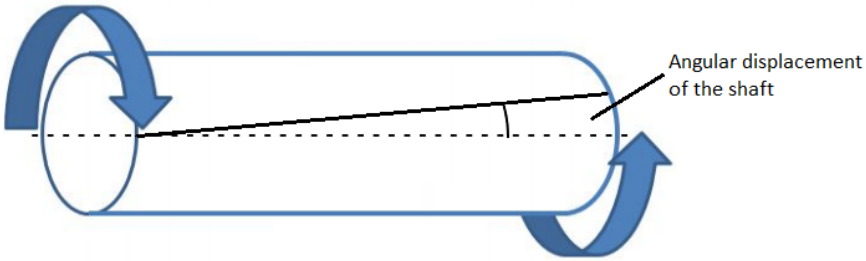

Figure 2. Basic principle of a twisted shaft [6].

Coupling with adjustable torsional stiffness. Fig. 3 presents the coupling and the main parts. The coupling consists of input and output halves at the ends, 6 beams, adjustable flange and middle shaft. The shaft of electric motor is attached to the input half. Torque is transferred from the input half through the beams to the adjustable flange. The flange transfers the torque to the middle shaft by spline. The middle shaft is fixed to the output half. The stiffness of the coupling is adjusted by moving the position of the adjustable flange along the middle shaft. When the flange is near the input half the stiffness of the coupling is high since the effective length of the beam is short. When the flange is moved towards the output half the effective length of the beams increases and the stiffness decreases.

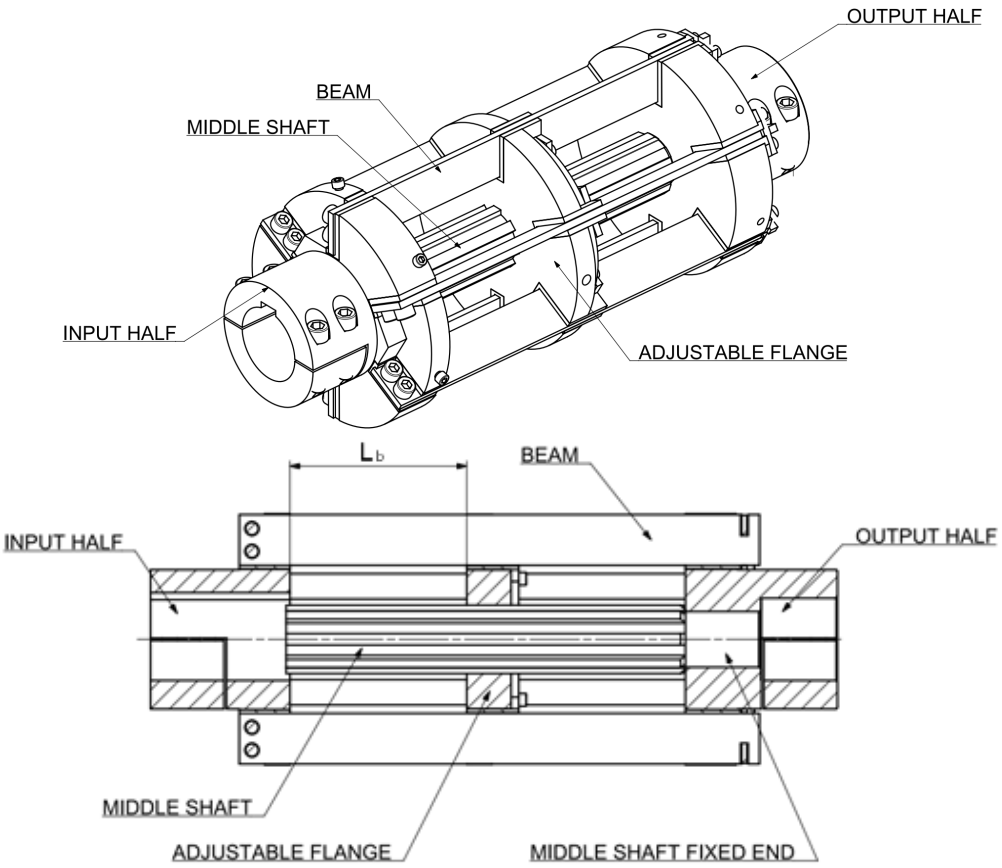

Figure 3. Coupling with adjustable torsional stiffness. L_b represents the effective length of the beams.

Analysis of the coupling with adjustable torsional stiffness

Analytical calculation of torsional stiffness. The coupling consisted of six beams and a spline as shown in Fig. 3. The beams were parallel, and stiffness of the beams was defined as shown in equation (1) in accordance with [7]. k_b corresponds to the input side of the adjustable flange while k_{bs} corresponds to the output side.

$$k_b = r \cdot 6 \cdot \frac{3EI}{{L_b}^3}, \quad k_{bs} = r \cdot 6 \cdot \frac{3EI}{(L-L_b)^3}. \tag{1}$$

Where L_b is the effective length of the beams, L is the total length of the beams, r is the distance between the center of the beam cross section and the center of the rotation, and E is the Young's modulus of the beams (Fig. 4). I is the second moment of inertia and it is defined as

$$I = \frac{bh^3}{12}, \tag{2}$$

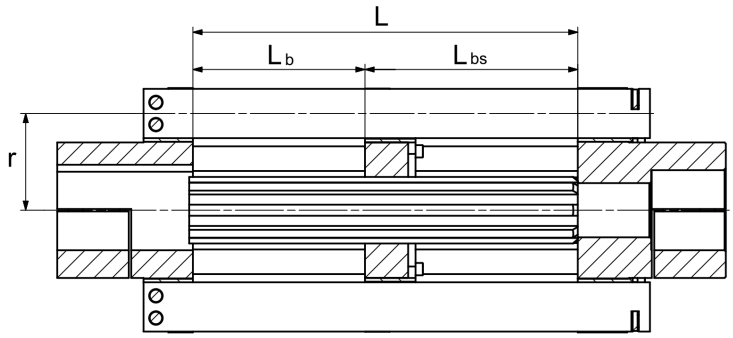

Figure 4. Dimensions used in the calculations.

where b is the width, and h is the height of the cross section of the beam. The stiffness of the shaft is defined in accordance with the torsional rigidity definition

$$k_s = \frac{GI_p}{L-L_b}, \tag{3}$$

where G is shear modulus. I_p is defined as

$$I_p = \frac{\pi d^4}{32}, \tag{4}$$

where d is the average diameter of the spline shaft.
The total stiffness of the coupling is obtained where effective length of the beams was in series with parallel spline shaft and rest of the beams.

$$k = \left(\frac{1}{k_b} + \frac{1}{k_{bs}+k_s}\right)^{-1} \tag{5}$$

The parameters used in the calculations are presented in Table 1. The effective length of the beams was changed in accordance with the adjustable flange position.

Table 1. Geometrical and material parameters used in the calculations.

Parameter	Radius r [mm]	Young's modulus E [GPa]	Shear modulus G [GPa]	Beam height h [mm]	Beam width b [mm]	Total beam length L [mm]	Spline shaft diameter d [mm]
Value	78.6	200	80	40	6	312	50

Simulated torsional stiffness. The coupling stiffness was also determined using Finite Element Method (FEM). The model was simplified by removing excess parts and geometry like screws, fillets and spline tooth.

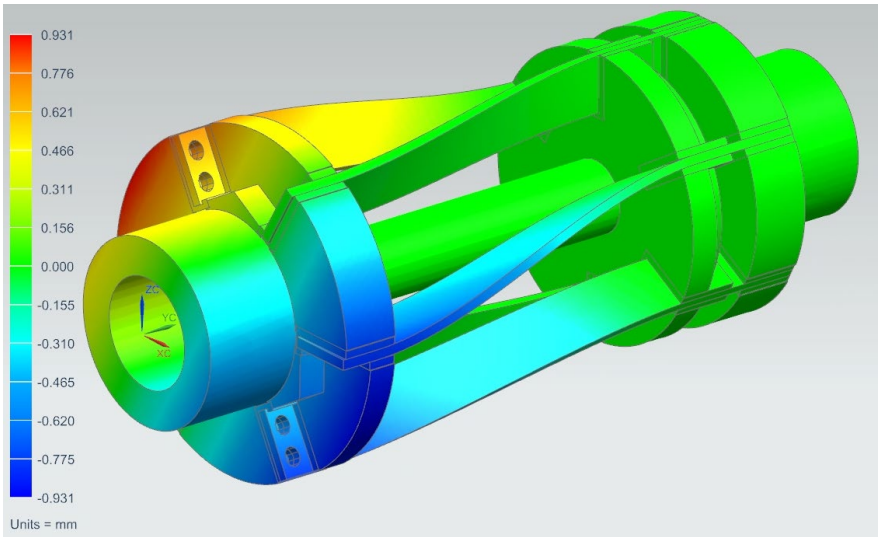

Figure 5. Result of a simulation with the coupling at the lowest stiffness. Deformation is exaggerated.

Experimentally measured torsional stiffness. The rotating angle was measured using a lathe as a test bench (Fig. 5). The input end of the coupling was attached to the lathe chuck to allow only torsional rotation. The output end was fixed. Torque was applied using weight and a calibrated torque wrench. Angular displacement was measured using a digital indicator. The torsional stiffness was calculated from the measured torque and the angular displacement.

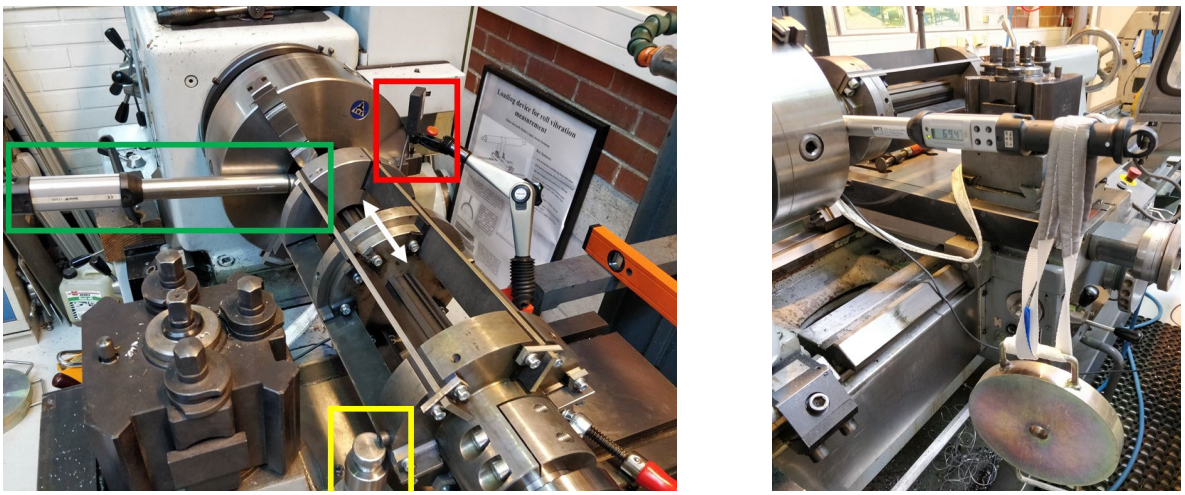

Figure 6. The test rig of the stiffness measurement (green: torque wrench, red: indicator measuring displacement, yellow: fixing device, white arrow: stiffness adjustment). On the right side, torque wrench with a weight.

The measurement process was completed as follows:
1) The adjustable flange was moved to the input end of the coupling, which is the stiffest point
2) Torque was applied, and the rotating angle was measured
3) Adjustable flange was moved towards the output end of the coupling to lower the stiffness
4) Steps 2–3 were repeated until the whole stiffness range of the coupling was measured

Torsional natural frequency analysis. In torsional vibration tests it was studied if the coupling has the capability to adjust the torsional natural frequencies of a rotating shaft line. The test configuration (Fig. 7) consisted of two electric motors, gearbox, rotor, elastomeric coupling, torque sensor and the coupling with adjustable torsional stiffness.

The driving electric motor with the gearbox was used to rotate the shaft line and the loading electric motor was used to produce torsional vibrations to the system. The elastomeric coupling connected the driving electric motor to the rotor and the coupling with adjustable torsional stiffness connected the loading electric motor to the rotor. Torque sensor was between the rotor and adjustable coupling, which was used to measure the torsional vibrations in the system.

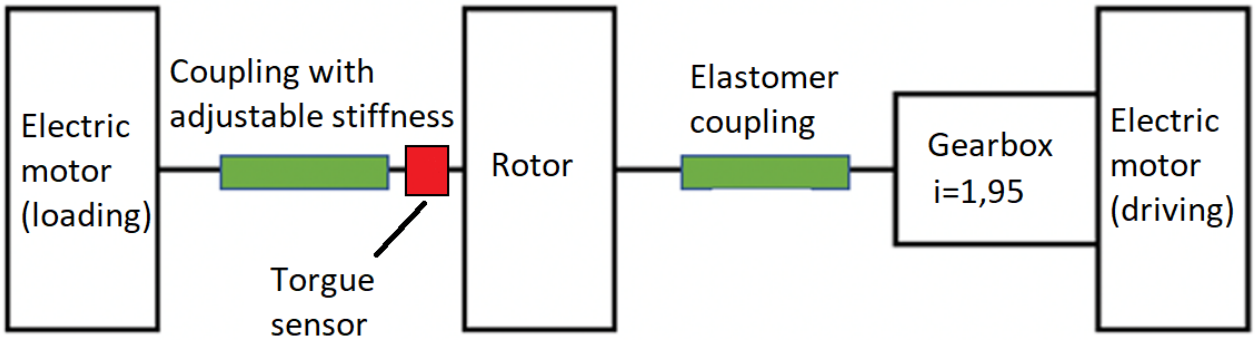

Figure 7.Test configuration for measuring torsional vibrations. From left: loading electric motor, the coupling with adjustable torsional stiffness, torque sensor, elastomeric coupling, gearbox, and driving electric motor.

The torsional vibration measurement process was completed as follows:
1) The adjustable flange was moved to the input end of the coupling, which is the stiffest point
2) Driving electric motor accelerated the shaft line to 10 revolutions per minute and it held the rotation constant
3) The loading electric motor was set to torsionally oscillate the shaft line at 1 Hz.
4) The oscillation torque was measured with the torque sensor
5) Torsional oscillation frequency was increased by 0.1 Hz increments
6) The oscillation torque was measured with the torque sensor
7) Steps 5–6 were repeated until the oscillation frequency was 50 Hz
8) Both motors were stopped, and the adjustable flange was moved towards the output end of the coupling to lower the stiffness
9) Steps 3–8 were repeated until the whole stiffness range of the coupling was measured

Results and conclusions

Coupling stiffness. The stiffness of the coupling was determined with analytical, simulated and experimental methods. The determined stiffnesses can be seen as function of the effective length of the beams in Fig. 6. The results were obtained considering an effective beam length range of 0-260 mm, which corresponds to the effective beam length. The measurements were done in 9 adjustable flange positions. The torsional stiffness values are presented in Table 2 and Table 3.

Table 2. Measured stiffness values and comparison to simulated stiffness values.

Adjustable flange position	Measured stiffness	Simulated stiffness	Measured to simulated stiffness ratio
[mm]	[Nm/rad]	[Nm/rad]	
0	45716	165450	28%
26	37590	142142	26%
57	27068	87259	31%
101	17045	39362	43%
151	11491	18000	63%
206	7969	11281	70%
260	6424	7670	80%

The measured stiffness values were much lower compared to the simulations (Table 2).

Table 3. Torsional stiffness values from analytical calculations and FEM simulation as a function of adjustable flange position.

Adjustable flange position	Analytical stiffness	Simulated stiffness	Analytical to simulated stiffness ratio
[mm]	[Nm/rad]	[Nm/rad]	
0	157837	165450	95%
26	169129	142142	119%
57	163831	87259	188%
101	106887	39362	271%
151	45141	18000	250%
206	22188	11281	197%
260	11450	7670	149%

The torsional stiffness decreases when the effective length L_b is increased (Fig. 8). The stiffness curve from analytical calculations and the FEM simulation are similar, but the curve from the analytical calculations has a larger slope and the stiffness is generally higher. The difference is likely caused by the analytical calculations being simplified. The formula used considers the force to be applied evenly to the beam. However, the torque load creates uneven loading to the beam surface, which also causes the beams to twist.

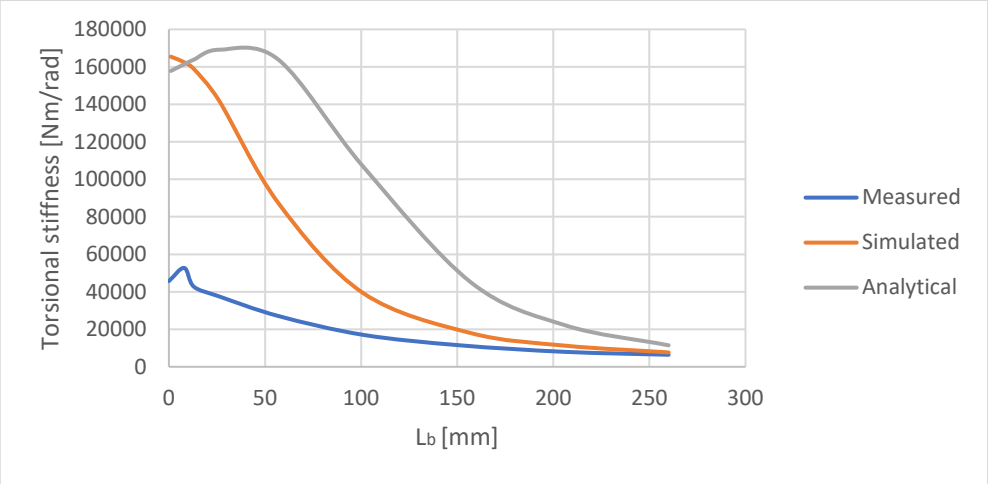

Figure 8. Analytical, simulated and experimental results of the coupling stiffness.

The measured torsional stiffness was much lower than simulated and calculated values, especially in the higher stiffness range. The phenomenon was deduced to be a caused by inaccuracies in the simulation and the measurement setup. The measurements should have been done in a proper measurement rig instead of the lathe.

Torsional natural frequencies. Torsional vibration tests were made to study if the coupling has the capability to adjust the torsional natural frequencies of a rotating system. As a result of the tests, the torsional natural frequency increased from approximately 15 Hz to 45 Hz when the torsional stiffness was adjusted. The measurement results are presented in Fig. 9. The figure presents measurements from 7 tests with different adjustable flange positions.

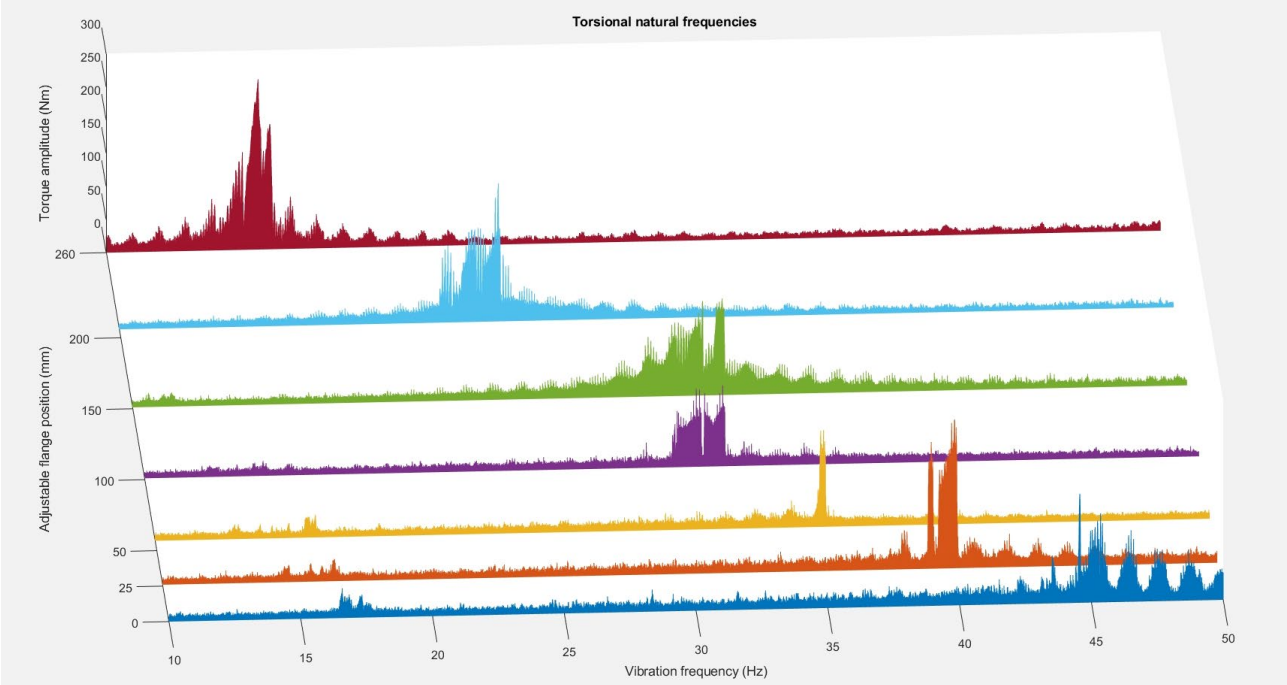

Figure 9. The measurement results from the vibration tests. The torsional natural frequency increases as the adjustable flange position decreases.

References

[1] Kelly, G. (2012). Mechanical Vibration Theory and Applications. (R. Adam, Ed.) (pp. 1–898). Nelson Education, Ltd.

[2] Ringfeder. (2015). New Coupling Design Offers Stiffness Adjustments. Viewed 6.2.2021. <https://blog.ringfeder.com/new-coupling-offers-stiffness-adjustments>

[3] Choi, J., Hong, S., Lee, W., Kang, S., & Kim, M. (2011). A Robot Joint with Variable Stiffness Using Leaf Springs. IEEE Transactions on Robotics, 27(2), 229–238.

[4] Urbansky, M. Comparison of piston and tangential pneumatic flexible shaft couplings in terms of high flexibility. Scientific Journal of Silesian University of Technology. Series Transport. 2018, 99, 193-203. ISSN: 0209-3324.

[5] Mobley, R. Keith, and R Keith Mobley. Vibration Fundamentals, Elsevier Science & Technology, 1999. ProQuest Ebook Central.

[6] Dewesoft, "Rotational and Torsional Vibration document," [Online]. Available: http://www.dewesoft.com/download. [Accessed 28.10.2013].

[7] Santaoja, K. 2019. Rasitusopin käsikirja. 5. uudistettu ja laajennettu painos. Espoo: Taras. ISBN 978-952-67899-7-2.

Elasto-Magnetic Load Measurement

Aku Hietala[1, a], Olli Partanen [1, b], Hung Nguyen [1, c], Panu Kiviluoma [1, d] and Petri Kuosmanen [1, e]

[1]Department of Mechanical Engineering, Aalto University, Finland

[a]aku.hietala@aalto.fi, [b]olli.partanen@aalto.fi, [c]phuong.h.nguyen@aalto.fi, [d]panu.kiviluoma@aalto.fi, [e]petri.kuosmanen@aalto.fi

Keywords: Elasto-magnetic, load measurement, crane, weighing method, EM-sensor

Abstract

The lifespan of cranes depends greatly on the total number of lifts and the amount of load that they handle. Load is commonly measured with strain gauges, which are glued to the measured object or integrated to load transducer. Elasto-magnetic (EM) phenomenon is an interesting non-contact method to measure load, which still needs further investigations to take full advantage of its potential. Goal of this study was to analyze the applicability of EM-method for load measurement in crane applications. The suitability was studied by performing laboratory tests to certify the relationship between sensor response and applied load. The EM-phenomena was found to work well in the capacity range of small cranes. There are also good possibilities to scale up the sensor for heavy loads.

Introduction

Load measurement is an essential part in the operation of load handling equipment such as cranes or fork-lifts. The lifespan of these equipment depends greatly on the total amount of lifts and the amount of load that they handle. With extensive load being applied, the lifespan of a crane reduces drastically. Accurate information about the measured load can be very useful for weight allocation in freight ships or in liquid manufacturing.

The most common technology that is currently employed for load measurement is strain gauge. It is a sensor which converts force, pressure, weight, or tension into a change in electrical resistance which can be measured by electrical devices. Strain gauge is also one of the most important sensors of electrical measurement technique applied to measurement of mechanical properties. Strain gauge has been used for stress analysis for decades [1].

One of the newer methods for load measurement is called Elasto-magnetic (EM) sensing. EM-sensor is based on magneto elastic phenomenon, where there is a direct correlation between magnetic properties and applied stress [2]. The EM-method has been proven promising for stress measurements in steel cable structures [3,4] and to be more sensitive method than strain gauge [2]. Goal of this study was to analyze the applicability of EM-method for load measurement in crane applications. In crane applications weight sensors are usually located in the carriage which brings its own challenges for installations and accuracy of the sensor. By applying the EM-sensor into the hook of the crane, the measurement comes closer to the weight and thus decreases the uncertainty.

Methods

Theoretical Model. When a ferromagnetic medium is placed inside a magnetic field H, the magnetic flux density B is related to H by the magnetic permeability $\boldsymbol{\mu}$ of the medium by the formula.

$$H = \mu B. \tag{1}$$

The magnetic permeability μ indicates the medium's resistant to magnetic field or how hard it is for the magnetic field to penetrate through the medium.

An elasto-magnetic sensor consists of two coils wound around a ferromagnetic bar. The input voltage in primary coil serves to generate magnetic field and magnetize the core. The induced voltage is measured by the circuit connected with the secondary coil.

Assuming that N is the number of rounds in secondary coil, μ_0 is the magnetic permeability of free space, and A_s, A_c are the cross-sectional areas of the secondary coil and the core, respectively. Then, according to Faraday's law, voltage induced in the coil is given by the change of the total magnetic flux penetrating through the coil over time. [5]

$$V_{ind}(t) = \left[NA_c \frac{\partial B(t)}{\partial t} + N(A_s - A_c)\mu_0 \frac{\partial H(t)}{\partial t}\right]. \quad (2)$$

Considering homogeneous magnetic field, the relative permeability of the core is measured as

$$\mu_r = 1 + \frac{A_s}{A_c}\left(\frac{V}{V_0} - 1\right). \quad (3)$$

Under stress application, the magnetic field of the core rotates and affects its magnetic permeability [5]. This implies that if stress is applied to the core of the above set-up, the output voltage V is expected to vary accordingly. Thus, the calibration of the output voltage under condition of varying applied force on the core would enable formulization of the relationship between them.

Affecting Factors. There are factors that affect the results and accuracy of the EM-sensor. These shall be taken in account when considering suitability of the EM-sensor for some specific applications. As seen from the Eq. 3, the relationship between permeability μ and induced output voltage V is linear. Induced voltage is sensitive to intensity of magnetization, cross-sectional area of the core, stress applied to the core, sensor manufacturing process and temperature [5].

Magnetization intensity factor can be eliminated by finding the optimal value for magnetic field strength *H*. Optimal value in this case means, that the *H* shall be high enough to saturate the core of the system. By reaching the optimal *H* value, the best sensitivity and linearity is obtained. To reach the saturation point requires more current, which generates more heat to the system. Heat and field strength *H* must be optimized to find the best performance level. [5].

Temperature effect can be analyzed by testing the setup with different temperatures of the test specimen and measuring the voltage change in the secondary coil. Temperature compensation is necessary so that the stress-permeability relation is dependent only to stress variations. These effects can be taken in account by using equation:

$$D\mu_r\,(T) = \; b\,(T - T_0). \quad (4)$$

Where b is temperature compensation factor (dV/dT). By adding this temperature compensation into permeability variation equation becomes:

$$D\mu_r(\sigma, T, T_0) = D\mu_r'(\sigma, T, T_0) + D\mu_r''(T) \; = \frac{A_s}{A_c}\left[\frac{V\,(\sigma, T) - V\,(0, T_0)}{V_0}\right] + b\,(T - T_0). \quad (5)$$

This equation shows the permeability relations due to stress and takes temperature variations into account. [5]. With these considerations only the effect of applied stress can be measured, from which a linear relationship between force and output voltage is expected as below:

$$F = F_0 + a(V - V_0) - b(T - T_0) \quad (6)$$

Where a = dF/dV and V_0 is the output at the reference load F_0 and at temperature T_0.

Test set-up. Elasto-magnetic sensor consists of two coils wound around nonmagnetic housing, that leaves round hole for the test specimen to go through. Primary coil is wound on top of the secondary coil. Coils have 200 and 50 rounds, respectively. Ferritic steel bar with radius of 10 mm was used as test specimen in this test and it was inserted through the sensor before mounting the set-up on the test bench. Schematics of the sensor is presented in Fig. 1.

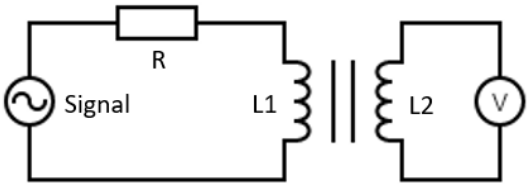

Figure 1. Construction of the EM-sensor.

Function generator and amplifier were used to excite the primary coil with a signal with frequency of 1 kHz and 0.6 A current. Data acquisition device was used to measure induced voltage and its change in the secondary coil. Thermocouple was also mounted on the test specimen to measure the temperature change during testing. Schematic drawing of the test set-up is presented in Fig. 2.

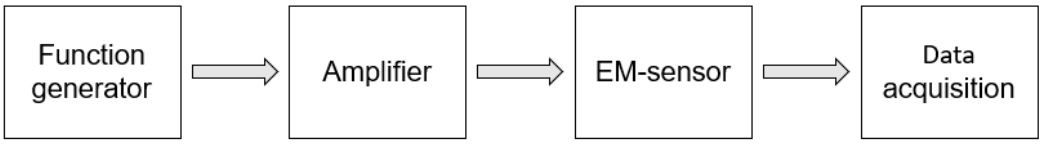

Figure 2. Schematics of the test set-up.

Before testing efficient performance of the sensor is tested with variable input voltages, with no load applied (Fig. 3.) Linear relationship of the output voltage proves the stable and efficient working of the sensing device. Current used in the tests is optimized to limit the heating of the sensing device and the test specimen, but still maintaining strong enough magnetic field.

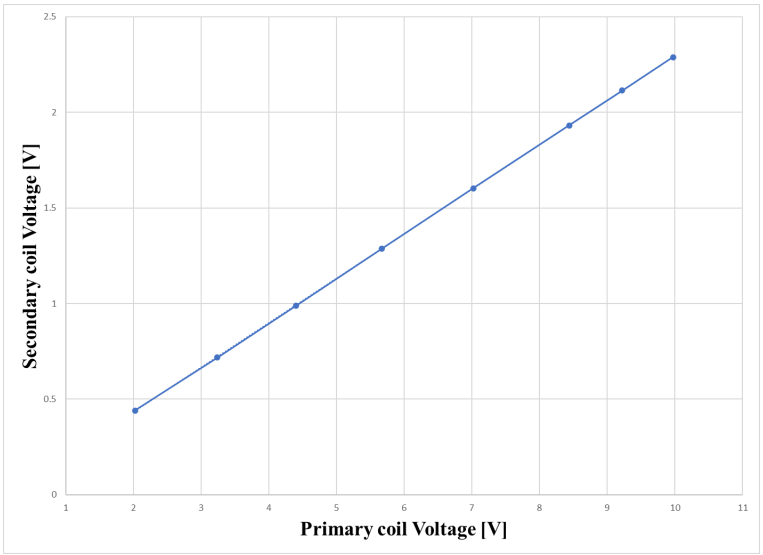

Figure 3. Relationship between the primary and secondary coil voltage.

Test procedure. For testing the changes in the induced voltage under stress of the bar tensile test bench MTS Insight with 30 kN load cell was used (Fig. 4.). First induced voltage was measured without any load to find out the zero state of the sensor. Then the test specimen was loaded with varying forces between 300 N to 15000 N and induced voltage over the secondary coil and temperature of the bar were recorded. Test was completed two times to ensure repeatability of the test. Factor a (dF/dV) was calculated from the test results, which gives the change in induced voltage in secondary coil corresponding to change in force applied. Temperature coefficient b (dV/dT) was measured during testing by measuring induced voltage in the secondary coil with varying temperatures of the bar. Factor b represents the change in voltage per change in temperature which enables temperature compensation of the bar during the use.

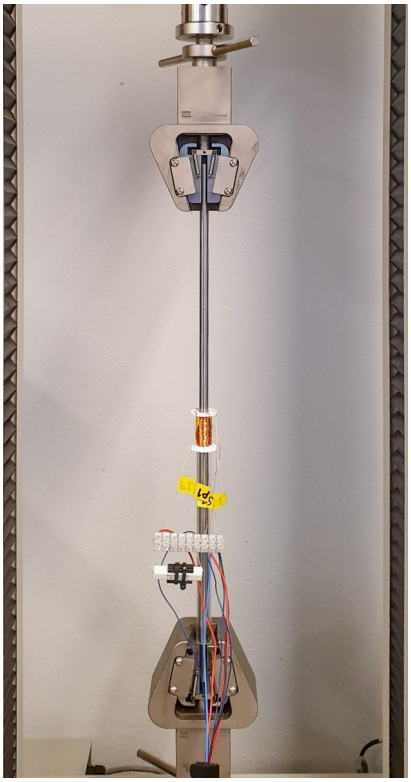

Figure 4. Test set-up in MTS Insight material testing device.

Results

From the test results of calibrating the sensor temperature coefficient of 0.00036 was determined and it was used to remove effect of the temperature change during the measurements. Relationship between force applied to the bar and change in output voltage is presented in Fig. 5. Linear relationship was not accomplished between force and output voltage, but a second order polynomial curve, with function of $y = 485782x^2 + 84218\text{x} + 112.74$, is fitted to the data of the two measurements. Correlation coefficient R^2 for the fitted curve is 0.999. With these measurements maximum absolute error of 289 N and average error percentage of 5.6% was calculated. Repeatability error of 0,069 % was achieved with two test runs with five equal measurement points.

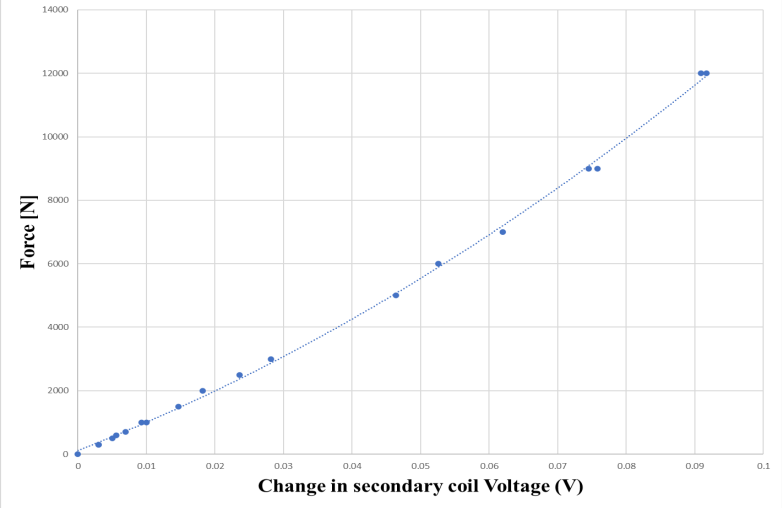

Figure 5. Relationship between load and secondary coil voltage

Conclusions

The calculated curve from testing the device did not come to be linear as expected. Eq. 6 does not apply to the solution. Equation must be modified to take the polynomial shape of the curve to account. When temperature change effected the voltage linearly, equation comes to be:

$$F = F_0 + a_1\big((V - V_0) - b(T - T_0)\big)^2 + a_2\big((V - V_0) - b(T - T_0)\big) + a_3 \quad (7)$$

In other EM-sensor related study, the linear dependency is achieved after 4000 kN load, which is not common level of load in crane industry [5]. In crane applications, loads mostly vary from 1 kN up to 1200 kN depending on the application. Lack of linearity does not mean that the EM-method cannot be used in crane applications. Since the setup is considered to have good repeatability and accuracy it is possible to use it for crane applications. If the behavior of the force and induced voltage follows the same function up to capacity of the crane, the load can be predicted from the voltage values. To have more precise accuracy rate of EM-method, Gage R&R study shall be performed under laboratory circumstances. However, with only few tests and temperature calibration the EM-sensor has repeatability error of 0,07 %, which is quite good compared to strain gauge -based load measurement device with ± 0,02 % repeatability [6].

For the test specimen to have such low thermal mass it was noticed to heat up significantly when the device was running. Even after optimizing the current for the system, during testing the temperature of the bar rose from 26 to 36 °C. With larger test specimen this change is going to be possibly smaller, but still significant enough to consider modifying the system to use voltage pulses to excite the primary coil, instead of the continuous AC-signal. Primary coil reacts on the change in the excitation current, which makes using pulses a possible solution. This would allow the system to use higher excitation current, without having thermal issues. [4]

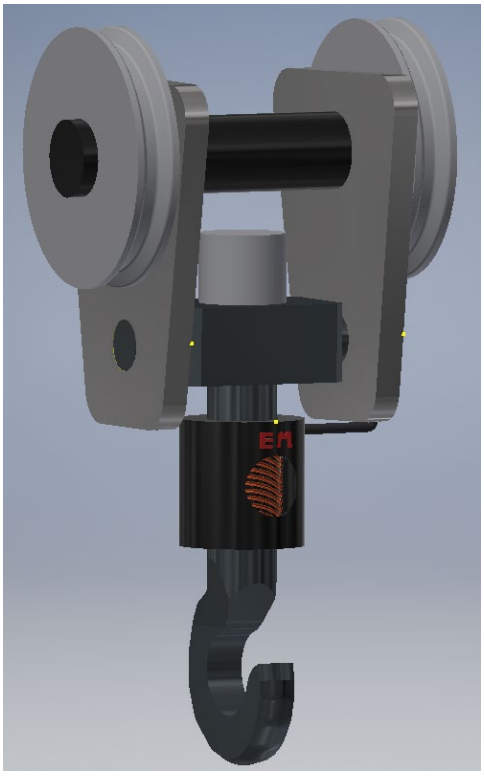

Figure 6. Crane hook.

The thicker the shank (Fig. 6) is, the larger and more powerful sensor unit is required to achieve the optimal field strength *H*. Also shank material has effect on the field strength and mechanical

limitations of the crane so it is important to consider suitable materials. In addition, crane applications are located indoors and outdoors with varying ambient temperatures. Thus, temperature calibration shall be done according to prevailing environmental conditions. For 40 mm diameter hook shank made of AISI1040 carbon steel, the EM-sensor would be about 75 mm long and it would have 1000 rounds on primary coil and 200 rounds on secondary coil. This EM-sensor would need approximately 90 amps to make the core saturated.

In many crane applications, the hook is quite like one shown in Fig. 6. In this study it has been thought that the EM-sensor could be installed to the hook shank. Sensor size depends on the shank length and diameter. This study does not express results about how much free space there should be before and after the sensor unit to avoid magnetic field errors caused by other steel or iron components.

After completing testing and research on elasto-magnetic sensing, it is considered as suitable solution to be used in the load measuring in overhead cranes. Measurement range for the sensor is wide enough to cover whole load range of different crane types and resolution of the sensor is accurate enough for most use cases of the cranes. With further development of the sensing device, accuracy of the sensor can still be improved and thus the errors to be decreased. For the next steps to develop the concept for crane applications the device needs to be scaled to more realistic use cases and the tests to be repeated.

References

[1] Hannah, R. and Reed, S., 1994. *Strain gage users' handbook*. London: Chapman & Hall.

[2] Yim, J., Wang, M., Shin, S., Yun, C., Jung, H., Kim, J. and Eem, S., 2013. Field application of elasto-magnetic stress sensors for monitoring of cable tension force in cable-stayed bridges. *Smart Structures and Systems*, 12(3_4), pp.2-13.

[3] Zhang, R., Duan, Y., Or, S. and Zhao, Y., 2014. Smart Elasto-Magneto-Electric (EME) Sensors for Stress Monitoring of Steel Cables: Design Theory and Experimental Validation. *Sensors*, 14(8), pp.13644-13660.

[4] Ren, L., Xiu, C., Li, H., Lu, Y., Wang, J. and Yao, X., 2018. Development of elasto-magnetic (EM) sensor for monitoring cable tension using an innovative ratio measurement method. *Smart Materials and Structures*, 27(11), pp. 2-3.

[5] Cappello, C., Zonta, D., Laasri, H., Glisic, B. and Wang, M., 2018. Calibration of Elasto-Magnetic Sensors on In-Service Cable-Stayed Bridges for Stress Monitoring. *Sensors*, 18 (2), 466. pp. 4-7.

[6] Library.e.abb.com. 2021. Robust and reliable Weighing systems for the heavy industries. [online] Available at: <https://library.e.abb.com/public/18cb86fe2dee419cabb8390ce5d1ba6a/3BDD016540-EN_B.pdf> [Accessed 5 April 2021].

Effects of Pressure and Air Flow on Drying Rate of Nano Paper

Tuukka Kasperi Virkki[1, a *], Po Wey Lim [1, b], Panu Kiviluoma[1,c], Petri Kuosmanen[1,d]

[1] Department of Mechanical Engineering, Aalto University, Finland

[a]tuukka.virkki@aalto.fi, [b]wey.lim@aalto.fi, [c]panu.kiviluoma@aalto.fi, [d]petri.kuosmanen@aalto.fi

Keywords: Nano paper; Drying; Nanocellulose; dewatering; Drying rate; Nanopulp; Pressure; Airflow

Abstract

This study investigates the dewatering and drying time of nanocellulose pulp in laboratory conditions. The dewatering is performed with a custom-built device that regulates the pressure to force pulp-water solution through a filter-plate. The dewatering and drying are done in two phases. Pressure on both sides of the filter plate and airflow through the system are measured during the dewatering and drying of nanocellulose. Research on the topic will be continued, but this paper introduces a proof of concept for a device that is capable of measuring required process parameters of the dewatering process.

Introduction

The motivation to research the drying process of smaller fibers, such as nanocellulose fibers arises from their unique properties. Nano fibers can be produced from agricultural waste, and with the right fabrication process, their tensile strength can be roughly half of structural steel [1]. In the paper industry, the critical and energy consuming part is the drying process of the paper [2]. This is due to water getting trapped in-between the paper fibers, making it much harder to dry. The removal of water is done with the help of temperature and pressure, forcing the water out and evaporating it [3]. The energy consumption of the drying process correlates with the size of the paper fibers; smaller fibers make cause the sheet of paper to dry slower as the porousness of the sheet decreases [4].

The paper industry has mainly done research on fibers much larger than nano size. Common produced paper may also contain other filler items such as ground calcium carbonate and precipitate calcium carbonate which do not help the sheet of paper to retain its strength when compared to nano cellulose filler [5]. This is one of the reasons to investigate the drying properties of nano fiber. There are also other possibilities such as manufacturing nano paper-based chips [6] and having nano paper as a new material for bioengineers.

The aim of this research was to determine how process parameters, such as pressure and airflow affect the drying rate of dewatered nano paper. A device and filter for nano paper dewatering were built to produce and dewater a nano paper sheet. The nano paper was manufactured in two steps. In the first phase the water and nano fibers were separated with the help of filter and pressure. Filter needs to be fine enough to catch nano fibers and pressure needs to be high enough to force the water through the filter. Without pressure the nano fibers would clog the filter and dewatering would not happen. In the second step the wet nano sheet was dried. During this step the pressure and air flow are measured to find out how they will affect the drying rate. In this step also heat can be added, as it is not necessary in the first step to create the sheet.

Methods

The device is a pressure chamber comprised of two glass cylinders [7] that are compressed together with four flanges - a top flange, two middle flanges and a bottom flange. The glass cylinders are compressed between the flanges with threaded rods that run the length of each glass cylinder. A filter plate is located between the middle flanges. Cross-section of the device is seen in Fig. 1. O-rings are used to ensure that the device is airtight. The top flange has an air inlet with a pressure regulator. The flange has also process connections for pressure and temperature sensors. The bottom flange has an air outlet with a draining valve to help empty the chamber of excess water. The air outlet also has a detachable measuring block with a pressure sensor, temperature sensor and an air flow sensor. This measuring block is connected to a laboratory vacuum system.

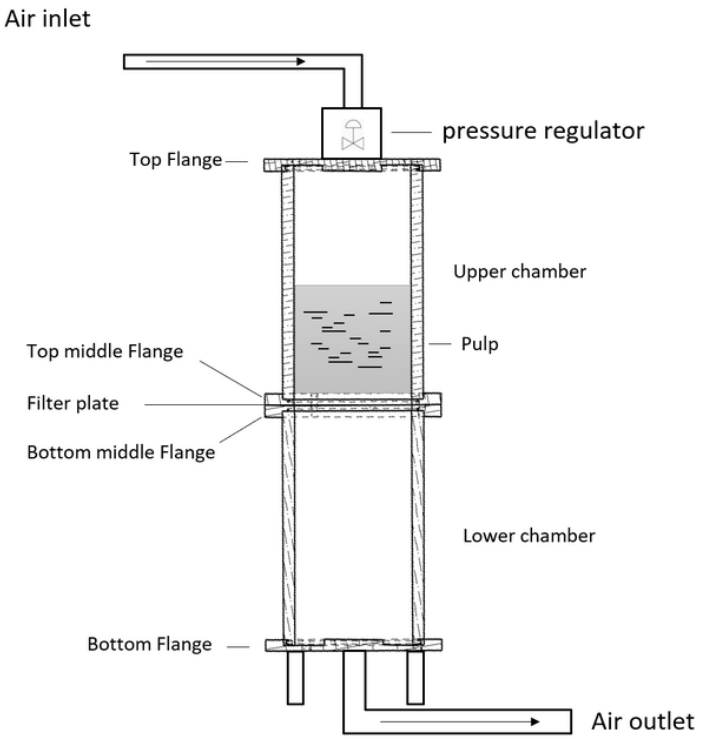

Figure 1. Simplified cross-section of the device. The filter plate is located between the middle flanges. The top flange has an air inlet with a pressure regulator and connections for pressure and temperature sensors. The bottom flange has an air outlet with a draining valve to help empty the chamber of excess water.

Process requirements

The maximum parameters of the research are shown in Table 1. Table 2 shows the selected sensors. DAQ (data acquisition) used for this research was NI USB-6001. It was important to see how different values in pressure would have an impact on the dewatering rate. Transparency of the walls was requested so that the process of nano sheet forming could be seen.

Table 1. Requirements of the device.

Pressure	2 bars
Temperature	22 °C
Inner diameter of glass cylinder	100 mm
Cylinder wall thickness	5 mm

Table 2. Measured quantities and chosen sensors.

Parameter **Sensor**	**Range**	**Accuracy**
Pressure upper chamber SMC PSE530-M5-L	0…1 MP	±2 % of F.S.
Pressure lower chamber SMC PSE531-M5	0…100 kPa	±2 % of F.S.
Airflow SMC PFM710-C6-E	0…10 SLPM (standard liters per minute)	±1 % of F.S.
Weight	0 – 100 g	0.01 g

In the first phase, 1000 ml of pulp with 30% of nano fibers was inserted into the upper chamber. The chamber was then be pressured up to 2 bars in room temperature to force the water through the filter into the lower chamber. It is recommended to keep the pressure as low as possible to minimize the stress on the filter plate. Excess pressure of 200 mbar was enough to dewater the pulp. When the water was forced through the filter, the nano fibers formed a wet sheet on the filter plate. Once all the water was drained to the lower chamber, both chambers will be emptied and dried of excess water. The formed nano sheet could be removed with the filter plate, weighed, and set back.

In the second phase, pressure was varied to detect the airflow in the process. Suction was also added to the lower chamber, creating a vacuum. After drying, the filter plate was weighed to determine the removed moisture content. In this case, phase two was more focused on investigating if the increased pressure reduced the drying time of the nano sheet at all rather than obtaining the exact amount of water removed.

Results

The pressure was adjusted through testing, and the test time was one hour. The dewatering time was 20 minutes, while the rest of the test time was spent on the attempt to dry the nanosheet. Adjusting the pressure can be seen in Fig. 2 which affected the airflow seen in Fig. 3. In steady state there is no variation in airflow as the nanosheet does not allow air to pass through. The detected airflow must then come from the lower chamber when the suction is increased, creating a higher vacuum.

Higher excessive pressures in the upper chamber were not found to shorten the dewatering time. This is due to the size of the holes in the filter plate and the water being trapped between the fibers. Preliminary tests showed that 2000 mbar of excessive pressure caused plastic deformation on the filter plate while also keeping the pulp dewatering time roughly at 20 minutes. The results were, however, invalidated and not recorded due to the plastic deformation of the plate. The system was fully sealed at time 3100 seconds in Fig. 2 and Fig. 3. Therefore gradual drop of airflow is not seen in timeframe 2650 s – 3060 s unlike in 3100s.

Without excessive pressure dewatering of nano pulp does not take place. Speed of the dewatering is linked to the amount of nano fiber in the pulp. A pulp that contained only 10% nano fibers dewatered in seconds with same excessive pressure of 200 mbar.

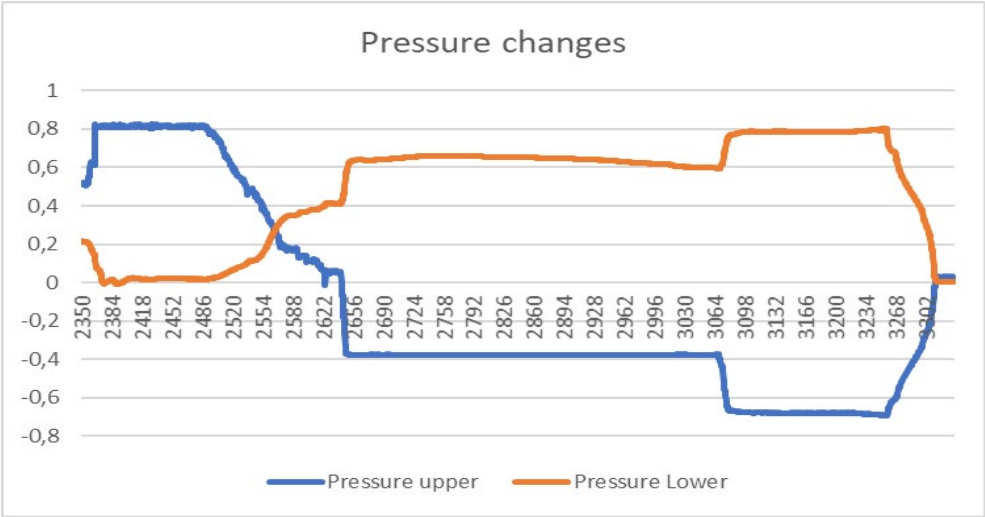

Fig 2. Pressure changes in phase 2.

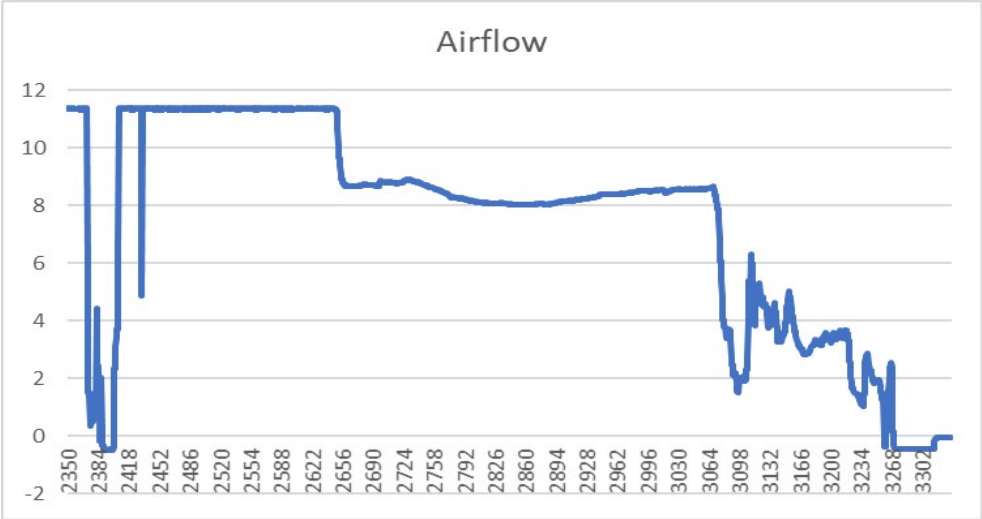

Fig 3. Changes in airflow.

Discussion

The pressure changes in forcing a change in airflow was expected. It was also expected that airflow would be zero in steady state. In contrast, it was unexpected that the dewatering and drying time was not correlating with the excessive pressure. This can be explained with the size of the holes and nano sheet being almost impermeable to air. As the holes clog, increase in pressure may not necessarily allow water to force its way through and the water is trapped in-between the fibers. This hypothesis is supported by the preliminary test where the filter plate bent beyond repair while the dewatering time was not reduced with high excessive pressure.

This study introduced a proof of concept for measuring process values in the dewatering and drying process of nano paper. For future research, installing air heaters may improve the drying time as evaporation happens more rapidly. In addition to the air heater, moisture and temperature sensors should also be introduced. Boiling temperatures might force evaporation of the trapped water droplets, drying the sheet. There might be, however, some issues with high excessive pressure in the upper chamber due to the boiling point of water being higher than 100 °C at pressures above one atmosphere. Regardless of these issues, increased temperature should improve the natural evaporation of the paper sheet. The next step could investigation of drying time of nano paper under high temperature and pressure.

References

[1] I. González, M. & Alcalà, G. & Chinga-Carrasco, F. & Vilaseca, S. & Boufi & P. Mutjé. From paper to nanopaper: evolution of mechanical and physical properties. Cellulose **21**. (2014). 2599–2609. [Viewed 9.2.2021]. https://doi.org/10.1007/s10570-014-0341-0

[2] Stenström, S. Drying of paper: A review 2000–2018. Drying Technology. (2019). **38**(7). 825-845. https://doi.org/10.1080/07373937.2019.1596949

[3] Hewitt, D. R. & Paterson, D. T. & Balmforth, N. J. & Martinez, D. M. Dewatering of fibre suspensions by pressure filtration. Physics of Fluids. (2016). **28**(6). [Viewed 9.2.2021] https://doi-org.libproxy.aalto.fi/10.1063/1.4952582

[4] Rantanen, J. & Maloney, T. C. Press dewatering and nip rewetting of paper containing nano- and microfibril cellulose. Nordic Pulp & Paper research Journal. (2013). **28**(4). 582-587. [Viewed 8.2.2021]. Available: https://doi.org/10.3183/npprj-2013-28-04-p582-587

[5] Das, A. K. & Islam, M. N. & Ashaduzzaman, M. & Nazhad, M. M. Nanocellulose: its applications, consequences and challenges in papermaking. Journal of Packaging Technology and Research. (2020). **4**(3). 253-260. [Viewed 8.2.2021]. https://doi.org/10.1007/s41783-020-00097-7

[6] Xu, Y. & Liu, M. & Kong, N. & Liu, J. Lab-on-paper micro- and nano-analytical devices: Fabrication, modification, detection and emerging applications. Microchim Acta **183**. (2016). 1521-1542. [Viewed 9.2.2021]. https://doi-org.libproxy.aalto.fi/10.1007/s00604-016-1841-4

[7] Ding, L. & Doss, K. & Yang, Y. et al. Volume relaxation in a borosilicate glass hot compressed by three different methods. J Am Ceram Soc. (2021). **104**(2). 816-823. [Viewed 9.2.2021]. https://doi-org.libproxy.aalto.fi/10.1111/jace.17482

Ultra-Wideband Localization for Crane-Robot Cooperation

Alexander Schüßler[1,a], David Wargh[2,b], Wanfu Zheng[2,c], Olli Laasonen[3,d], Nilusha Jayawickrama[1,e], Panu Kiviluoma[1,f] and Petri Kuosmanen[1,g]

[1]Department of Mechanical Engineering, Aalto University, Finland

[2]Department of Electrical Engineering and Automation, Aalto University, Finland

[3]Noccela Oy, Finland

[a]alexander.schussler@aalto.fi, [b]david.wargh@aalto.fi, [c]wanfu.zheng@aalto.fi, [d]olli.laasonen@noccela.fi, [e]nilusha.jayawickrama@aalto.fi, [f]panu.kiviluoma@aalto.fi, [g]petri.kuosmanen@aalto.fi

Keywords: IoT, Industry 4.0, automated material flow, machine-robot interaction, UWB, ROS

Abstract

With the increasing automation of manufacturing and logistics, large number of robots, automated machines and automated cranes will operate in indoor environments. Due to the lack of global navigation satellite systems (GNSS) in indoor environments, safe localization of robots and machines remains a great challenge. In this study, the use of an ultra-wideband system for the indoor localization of robots and machines was investigated. The cooperation between a crane and a robot was examined as an exemplary process. A commercially available ultra-wideband system was integrated into the Robot Operating System (ROS) to localize the robot and the crane. The presented system was validated with a one-dimensional following situation between the crane and the robot. The trajectories of the robot and the crane demonstrate the capability of the presented system. Overall, the research indicates that ultra-wideband systems can be used as an indoor localization method for automated material flow processes.

Introduction

The digitalization and automation of manufacturing and logistics is increasing rapidly with the rising trend of Internet of Things (IoT) in industrial environments. According to the Statista In-depth: Industry 4.0 2020 digital market outlook [1] the globally installed base of IoT connected devices will increase by 17% from 2019 to 2025. As a result, an increasing number of robots, automated machines and automated cranes will be used in the manufacturing and logistics process. With the lack of a global navigation satellite systems (GNSS) in indoor environments, safe localization of moving robots and machines remains a great challenge. Localization through ultra-wideband (UWB) systems is seen as a promising replacement for GNSS in indoor environments. These UWB systems consist of multiple beacons located at the room's ceiling and tags placed on the moving robots, machines and cranes that need to be localized. The beacons at the ceiling send radio signals, which get reflected by the tags on the moving objects. The time of flight between sending the radio signal and receiving the reflected UWB signal can be measured and used to determine the location of the tag. There are different methods to calculate the position of the tag like Two Way Ranging (TWR) or Time Difference of Arrival (TDoA). A great advantage of UWB systems for indoor localization is the decreasing cost per robot with an increasing number of operating robots in one room due to the low cost of additional tags. Another benefit of the UWB system is the possibility of retrofitting old machines, which can be included into the automated manufacturing and logistics process trough adding an inexpensive tag.

The use of UWB systems for localizing indoor robots has been previously studied with various approaches to the problem. Krishnan *et al.* [2] proposed an impulse-radio (IR) based UWB system

for indoor robot navigation. A ceiling mounted reader antenna and a mobile tag antenna on the robot are used to navigate a single robot in an indoor environment. Their results show that IR-UWB provides robust localization of robots. Similarly, Segura *et al.* [3] presented a localization system based on IR-UWB sensors. In their work, they described a novel time of arrival estimation algorithm to improve the localization accuracy. Their study shows that UWB sensors can accurately locate mobile robots in indoor environments. The combination of UWB systems with additional sensors through sensor fusion is the most common approach to improve the localization accuracy. Current methods based on sensor fusion often include the combination of UWB positioning and odometry from wheel encoders. Dwek *et al.* [4] and Chengbo *et al.* [5] used an extended Kalman filter to combine UWB sensor data and odometry data for improved localization accuracy and robustness. A linear Bayesian filter to combine UWB position measurement and odometry is introduced by Zhang et al. [6]. Sadruddin *et al.* [7] increased the indoor localization accuracy by combining stereo vision data, inertial measurement unit (IMU) data and UWB position data with an extended Kalman filter. In addition to localizing the robots the avoidance of obstacles is necessary to ensure safe navigation. Sbîrna *et al.* [8] combined an UWB localization system with ultrasonic sensors for obstacle avoidance.

The cooperation of cranes and mobile robots is a very common process step of the material flow during manufacturing. Current methods for the cooperation of cranes and robots include mainly vision-based systems. Ling *et al.* [9] proposed a visual tracking system for wheeled mobile robots and three-dimensional cranes. The system is validated by investigating an exemplary cooperation procedure. The crane is thereby following the robot's trajectory. A vision-based system for automated material handling in factories is presented by Lee *et al.* [10]. In their work, they are including an interface for a human operator, who can influence the material handling process. The use of an UWB localization system is a promising option to improve the automation of the material flow processes and therefore needs further investigation.

This study evaluates the usage of a low-cost and commercially available UWB localization system for the cooperation of cranes and robots. The proposed method is validated by a one-dimensional following situation between the crane and the robot. The localization system and control algorithms are implemented in the Robot Operating System (ROS) [11].

Methods

Overall setup. The overall system consists of a wheeled robot, a manually operated overhead crane and an ultra-wideband localization system and is realized in a laboratory environment. The UWB beacons are mounted to the laboratory ceiling. The tags are placed on the robot and the crane hook.

UWB system. The used ultra-wideband localization system is a commercially available system. Fig. 1 shows the complete overview of the localization system. The location of a tag is determined by measuring the time of flight of ultra-wideband signals between the beacons on the ceiling and the tags on the moving objects. The measurement data is transferred from the beacons to the Noccela cloud. A localization engine then calculates the position data from the measurements. The location data can be accessed in real-time or afterwards for further use. The blueprint of the laboratory is shown in Fig. 2. The six, active beacons are presented as green dots. To guarantee an accurate location of a tag, it needs a connection to at least three beacons. Therefore, the beacons are mounted in two triangular shapes in the working area of the laboratory.

Robot system. The used robot is a small, simple build wheeled robot with two wheels per side, which is mainly designed for research purposes. A Raspberry Pi 4 as the main computing unit and an Arduino as the motor controller are used in conjunction to control the robot. The data flow between the different robot subsystems is shown in Fig. 3. The UWB location data of the robot and the crane is retrieved from the Noccela cloud through a WebSocket. A WebSocket is a continuous connection between the server and client. The client and server communicate through a TCP/IP socket connection

[13]. By sending requests from the client to the server, it is possible to retrieve data from the server, which in this case is location data of the UWB tags. Before using the location data to control the robot

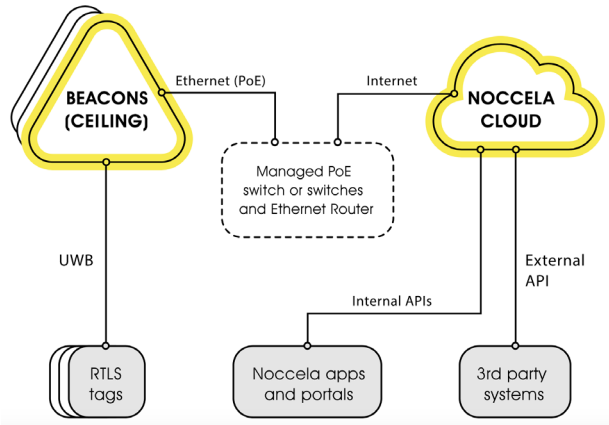

Figure 1. Overview of the Noccela UWB system [11].

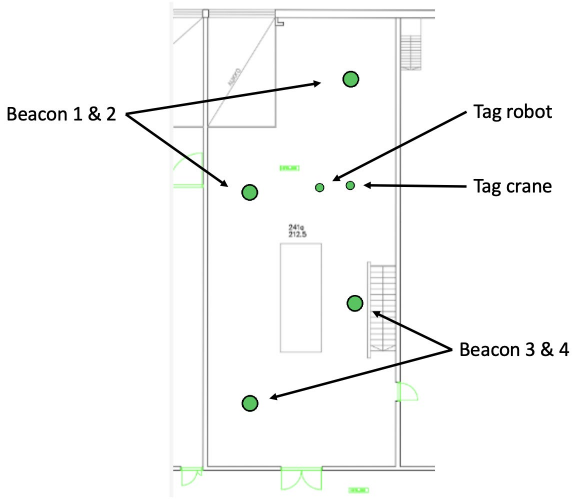

Figure 2. Laboratory blueprint.

movement, the data is filtered by building the average of ten data points. The used control algorithm is a bang-bang control with three states (forwards, backwards and stop). The control software is based on the Robot Operating System (ROS) [11], which is a very popular, open-source operating system for robots. Due to its modularity, ROS allows an easy integration of new components like the used UWB positioning system. The proposed ROS code structure for the robot is presented in Fig. 4. A ROS Master coordinates the nodes, which are the main building blocks of the ROS code. The nodes are the UWB WebSocket, the navigation algorithm and the Arduino. The communicated data between the nodes are called topics, which can be published by a node or a node can subscribe to them. The UWB WebSocket publishes the position data through the \uwb topic. The navigation algorithm retrieves the UWB position data through subscribing to the \uwb topic. It publishes the high-level control values through the topic \cmd. The Arduino receives the control values for the motor control through subscribing to the \cmd topic.

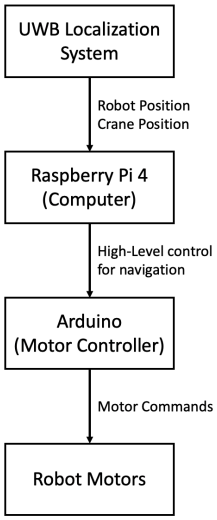

Figure 3. Data flow between the subsystems.

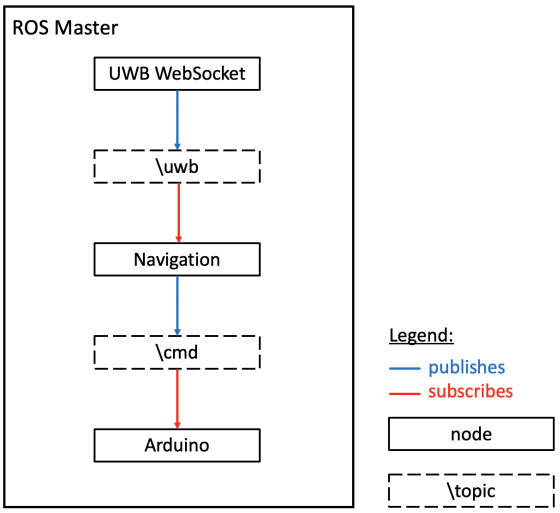

Figure 4. Structure of the ROS control software.

Testing procedure. The proposed localization method for the cooperation of cranes and robots was validated through a simplified scenario. The testing procedure is summarized in Table 1. The crane-robot cooperation scenario is simplified by investigating a one-dimensional following situation between the robot and the crane. The scenario represents a simplified material loading process of an autonomous platform by an overhead crane. The overhead crane trolley is manually moved in a

straight line by a human operating the remote control. With the change of the crane's position, the robot starts to move and follow the crane. The crane is then stopped by the human operator and the robot places itself under the crane trolley. After waiting at the virtual loading position, the crane trolley is moved back to its original position. The robot will change its driving direction and follows to crane to the original starting position. The real-time UWB position data of the robot and the crane are captured and saved. Therefore, the trajectories of the robot and the crane can be validated.

Table 1. Steps for one cycle of the testing procedure.

Step	Description
1	Overhead crane is moved.
2	Robot follows the crane.
3	Crane is stopped.
4	Robot stops under the crane.
5	Crane is moved back to the starting position.
6	Robot follows the crane to the starting position.

Results

The trajectories of the robot and the crane are presented in Fig. 5. The figure shows five cycles of the testing procedure. It is visible that the robot is following the crane with a slight delay. The average delay is about 1.75 seconds. There is an overshoot of the robot's trajectory at the locations, where a change of driving direction occurs. The average overshoot is around 290 mm. Overall, the trajectories indicate that the robot is able to follow the crane by using an UWB localization system as the sensor.

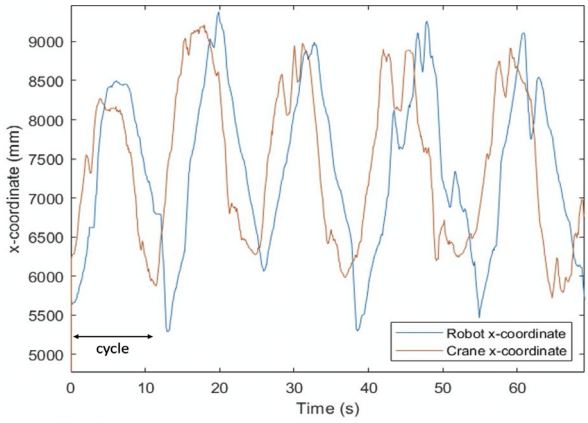

Figure 5. Trajectories of the robot and the crane for five testing cycles.

Discussion

In this research, an ultra-wideband system was used to localize moving robots and cranes for material flow processes. The results show the feasibility of using the system for a one-dimensional following situation. The delay and overshoot of the robot's trajectory are mainly a result of the simple control algorithm and filtering method that was used. By improving the control algorithm and the filter technique, the delay and overshoot of the robot could be decreased. The results proof that the proposed system can be used for the cooperation of cranes and robots in a laboratory environment. The proposed system could also be applied to other manufacturing and logistics processes, where moving robots and machines need to be localized. The next step of this research study is the increase of complexity of the cooperation process. The small, research-oriented robot needs to be replaced by an industrial robot platform that can transport material. The robot should also be able to detect and avoid obstacles. The overhead crane can be automated to enable a fully automated crane-robot cooperation. The whole crane-robot cooperation procedure should be expanded to a three-

dimensional material flow procedure. The improved system should then be applied to a real manufacturing or logistics process to improve the automation of material flow processes.

Acknowledgment

We acknowledge Noccela for providing us with their system and for supporting us throughout the whole project. We want to thank Risto Ojala for his support as an additional supervisor.

References

[1] D. Mehta, A. Hamke, L. Senn, In-depth: Industry 4.0 2020, Statista Digital Market Outlook, September 2020

[2] S. Krishnan, P. Sharma, Z. Guoping and O. H. Woon, A UWB based Localization System for Indoor Robot Navigation, 2007 IEEE International Conference on Ultra-Wideband, Singapore, 2007, pp. 77-82, doi: 10.1109/ICUWB.2007.4380919.

[3] M. J. Segura, V. A. Mut and H. D. Patiño, Mobile robot self-localization system using IR-UWB sensor in indoor environments, 2009 IEEE International Workshop on Robotic and Sensors Environments, Lecco, Italy, 2009, pp. 29-34, doi: 10.1109/ROSE.2009.5355978.

[4] N. Dwek et al., Improving the Accuracy and Robustness of Ultra-Wideband Localization Through Sensor Fusion and Outlier Detection, IEEE Robotics and Automation Letters, Jan. 2020, vol. 5, no. 1, pp. 32-39, doi: 10.1109/LRA.2019.2943821.

[5] K. Chengbo, Y. Huibin, Y. Juan and L. Wenchao, Research on Wheeled Mobile Robot Positioning Based on EKF Multi-sensor Data Fusion, 2019 3rd International Conference on Electronic Information Technology and Computer Engineering (EITCE), Xiamen, China, 2019, pp. 457-460, doi: 10.1109/EITCE47263.2019.9095173.

[6] S. Zhang, R. Han, W. Huang, S. Wang and Q. Hao, Linear Bayesian Filter Based Low-Cost UWB Systems for Indoor Mobile Robot Localization, 2018 IEEE SENSORS, New Delhi, India, 2018, pp. 1-4, doi: 10.1109/ICSENS.2018.8589829.

[7] H. Sadruddin, A. Mahmoud and M. Atia, An Indoor Navigation System using Stereo Vision, IMU and UWB Sensor Fusion, 2019 IEEE SENSORS, Montreal, QC, Canada, 2019, pp. 1-4, doi: 10.1109/SENSORS43011.2019.8956942.

[8] S. Sbîrnă and L. Sbîrnă, Optimization of indoor localization of Automated Guided Vehicles using ultra-wideband wireless positioning sensors, 2019 23rd International Conference on System Theory, Control and Computing (ICSTCC), Sinaia, Romania, 2019, pp. 504-509, doi: 10.1109/ICSTCC.2019.8885684.

[9] J. Ling, Y. Li and Y. Jia, Visual tracking strategy of a wheeled mobile robot and a multi-DOF crane equipped with a camera, Proceedings of the 32nd Chinese Control Conference, Xi'an, China, 2013, pp. 5489-5493.

[10] S. -J. Lee et al., Design of the Operator Tracing Robot for Material Handling, 2019 International Conference on Information and Communication Technology Convergence (ICTC), Jeju, Korea (South), 2019, pp. 1254-1256, doi: 10.1109/ICTC46691.2019.8939957.

[11] Open Source Robotics Foundation Inc., ROS, accessed 7 April 2021, https://www.ros.org

[12] Noccela Oy, accessed 7 April 2021, https://www.noccela.com/#about

[13] Sookocheff K., Sookocheff.com, How Do Websockets Work?, accessed 29 March 2021, https://sookocheff.com/post/networking/how-do-websockets-work/

Improving Tunnel Mode Efficiency of a Combined Azimuth Thruster

Jan Gregor[1,a *], Alpo Kuusisto[2,b] and Janne Mattila[2,c]

[1]Faculty of Mechanical Engineering, Czech Technical University, Czech Republic

[2]Department of Mechanical Engineering, Aalto University, Finland

[a]Jan.Gregor@fs.cvut.cz, [b]alpo.kuusisto@aalto.fi, [c]janne.a.mattila@aalto.fi

Keywords: CFD simulations, energy efficiency, propulsion system

Abstract

The azimuth thrusters are commonly used type of propulsion. This study focuses on a combined azimuth thruster and ways how to improve its efficiency in one of two operation modes, a tunnel mode. The research of existing solutions was made. Using preliminary computational fluid dynamics (CFD) simulations, the problematic issues were identified, and alternative construction of the thruster's assembly was proposed. The improved design behaviour was examined with CFD simulations and results of the efficiency improvement were presented.

Introduction

For medium and large ships and tugboats, a rotatable azimuth thruster protruding from the ship's bottom is a common and efficient means of steering and positioning [1]. For shallow water harbor operations, the thruster needs to be retracted inside the hull [2]. In that mode the thruster can still be used for steering if it is mounted inside a tunnel traversing the ship hull as in Fig. 1. Efficient design is different for these two operation modes. Current designs perform well in the open water, which is the main operation mode and prioritized. Better performance in the tunnel mode would mean more efficient steering, reduced fuel costs and reduced stresses on the thruster and ship structures. Due to the large scale of ships even small relative improvements can scale up to substantial absolute fuel savings.

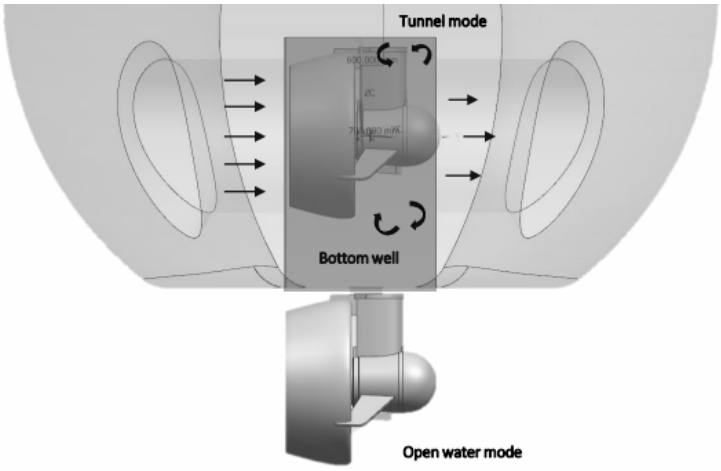

Figure 1. Combined azimuth thruster in two operation modes.

Known solutions of the problem are thruster shapes optimized for the tunnel mode and separate thrusters for tunnel [3] and open water mode [4, 5, 6], with penalties of reduced performance in the open water mode or additional costs, respectively. Options examined in this study include re-shaping the static tunnel section and flow control with movable elements. Research was focused on computational fluid modeling and analysis [7]. Actual structures are very large and careful analysis is required before building test models or prototypes.

The goal was to examine how the changes in the construction affect the flow in the tunnel mode. CFD simulations and testing of scaled model were used to validate the improvement.

Methods

The problem of the current design solutions of the azimuth thruster is that it has satisfactory efficiency just in the one of the operating modes. Ships spend most of the operation time in the open water mode and because of that the design with a good efficiency in the open water mode and non-satisfactory efficiency in the tunnel water mode was considered as a starting point. Problem, when operating in the tunnel mode, is that a considerable amount of the water flow loses its kinetic energy because of eddy turbulence. Flow diverts into the bottom well of the tunnel and does not contribute to the creation of the thrust. Considering that, the goal of the design was to make most of the water flow to continue inside the tunnel, minimize leakage through the bottom well and minimize energy losses.

2D CFD simulations. To understand better the behaviour of the water flow in the tunnel mode, 2D simulations in two perpendicular planes were examined. These simulations were very useful to make preliminary and quick simulations for understanding the system behaviour. Depending on details and boundary conditions results can vary much. The first horizontal plane simulations did not show any critical issues on design (Fig. 2 left). After that, vertical plane simulation (Fig 2. right) was inspected and was found out that quite a lot of the flow is going underside.

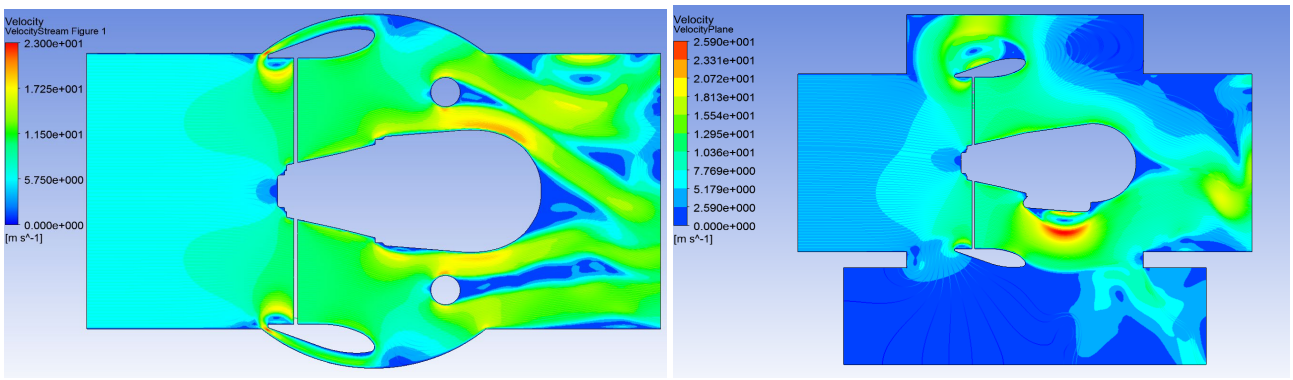

Figure 2. Flow streamlines and actual velocity in points of horizontal plane (left hand-side) and of vertical plane (right hand-side) in the tunnel mode.

Design for improved efficiency in tunnel mode. After initial results from 2D simulations, the most effective candidates for flow streamlining were selected for detailed modelling and 3D simulations. These were carried on together as an iterative loop, with gradual improvements. It was practical to have two parallel versions of the model file. A more detailed one for verifying all details were structurally viable and a simplified version for CFD simulations, as this reduced time for each simulation run. Quick simulations enabled more iterations, so details were added only as solutions were refined.

To achieve better efficiency in the tunnel mode the thruster assembly was equipped with additional static barriers and one moveable flap inside the tunnel chamber (Fig. 3). All the parts were designed in a way to avoid collisions with the thruster when retracting the thruster up and down. The main goal was to prevent the leakage through the bottom well and to avoid the flow circulation around the thruster nozzle. The moveable flap, closing the bottom well, can rotate 180 degrees around a hinge placed in the right-side wall of the thruster hub. Thanks to that design, during the operation in the open water mode the flap merges with the body of the ship and when the thruster is retracted up to the tunnel mode the flap moves to the closed position. All these proposed additional parts can be manufactured from the same material as the ship hull and they do not have any specific requirements, only resistance against the sea environment solved by anti-corrosion layers on the surfaces of the parts.

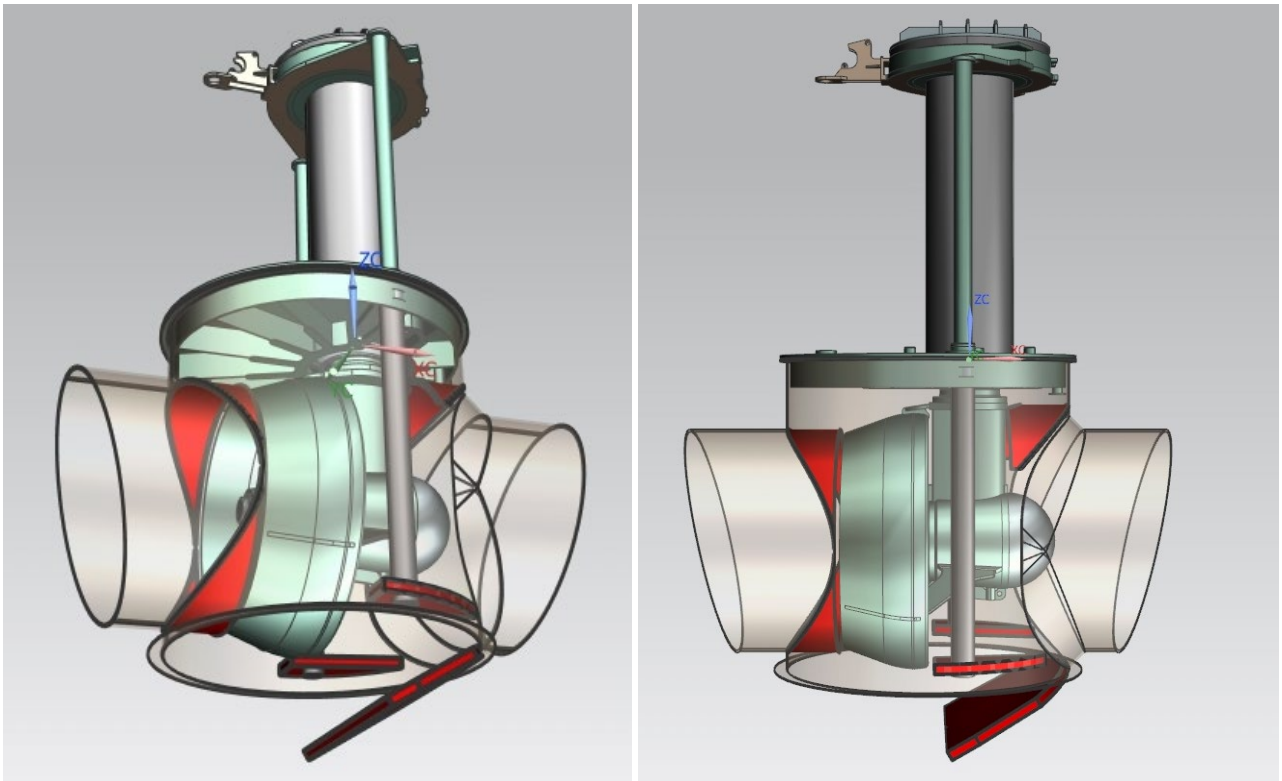

Figure 3. CAD model of the improved design, static barriers (tunnel extensions and parts helping to close the bottom well) and moveable flap in the bottom well are marked with red colour, moveable flap is displayed in half-open/half-close position.

3D Computational Fluid Dynamic simulation generally has several steps to be followed.

Modelling the desired shape in CAD program, including the fluid volume to be examined for the flow. Reasonable boundaries of the volume are essential for obtaining useful results. For open sea mode, this type of calculations includes a large water mass around the thruster, possibly extending beyond ship width. As objective of this research is not to obtain absolute efficiencies but to compare few tunnel mode solutions, the boundaries were set to the tunnel openings.

Division of the volume to a three-dimensional mesh for finite element calculations. Mesh density can be varying, with less details in open areas and more details close to solid bodies and especially edges of these. After first simulation runs, the gradient in relevant parameters like velocity, pressure, or vorticity hints where a denser mesh is necessary. Abrupt changes in values call for denser meshing.

Determining boundary conditions. What are the external pressures and flows? What is the driving force/s of the fluid flow? Careful selection of boundary conditions determines the usefulness of many simulation types and this applies to CFD as well. For sea water, also temperature and salinity may have notable effect for detailed simulations.

Setting flow estimation models like wall frictions and turbulence modelling. Turbulence especially is a phenomenon without explicit mathematical solution. All models describing it are rough approximations. Detail level of selected model drastically effects required calculation resources and result quality.

Analysing the results. The simulation results need to be comparable numerically to enable optimization of construction.

Scaled model was built for two purposes. At first, to understand better the whole assembly and at second, to be able to make an experimental setup for validation of the simulation results in the future.

Results

From the CFD simulations, the velocity fields of the flow inside the tunnel were used for examination of results. The thruster performance improvement was measured by velocity magnitude in the outlet. In Fig. 4 is shown small improvement of the thrust. Although, the thrust in forward direction was already satisfactory. In the initial design a lot of water was sucked through the bottom well. This effect and circulation in the upper part of the ship hull were suppressed by the flap and barriers. The main difference is that the thrust is more equally distributed over the tunnel.

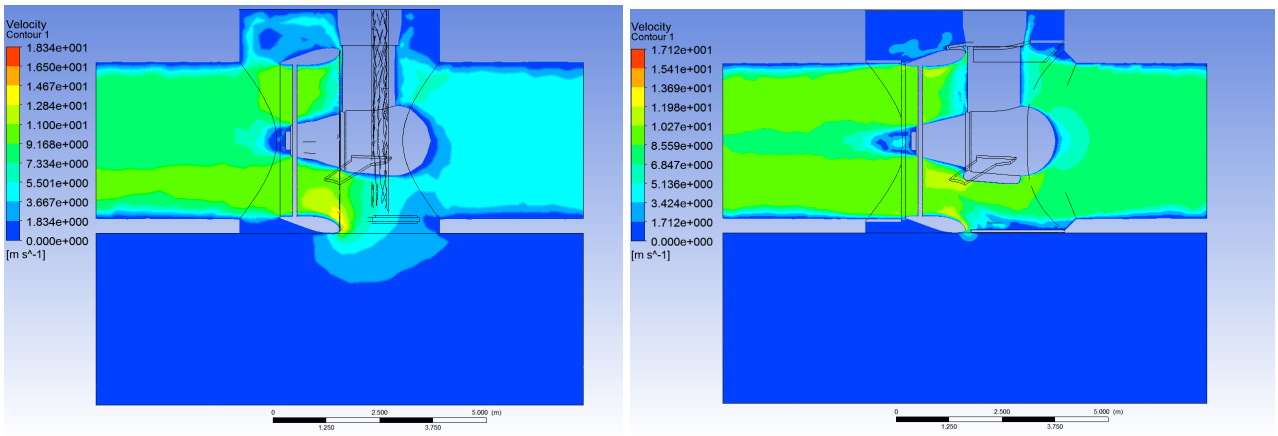

Figure 4. CFD simulation results in the forward direction, plots display a velocity field of flow, on the left is behaviour of the initial design, on the right is the improved design, which is about 5 % more efficient.

A significant improvement in the backward direction is shown in Fig. 5. In the initial design, the poor efficiency is caused mainly by circulations and by water leakage before and after the thruster through the bottom well. Suppressing of these factors was the key aspect for efficiency improvement.

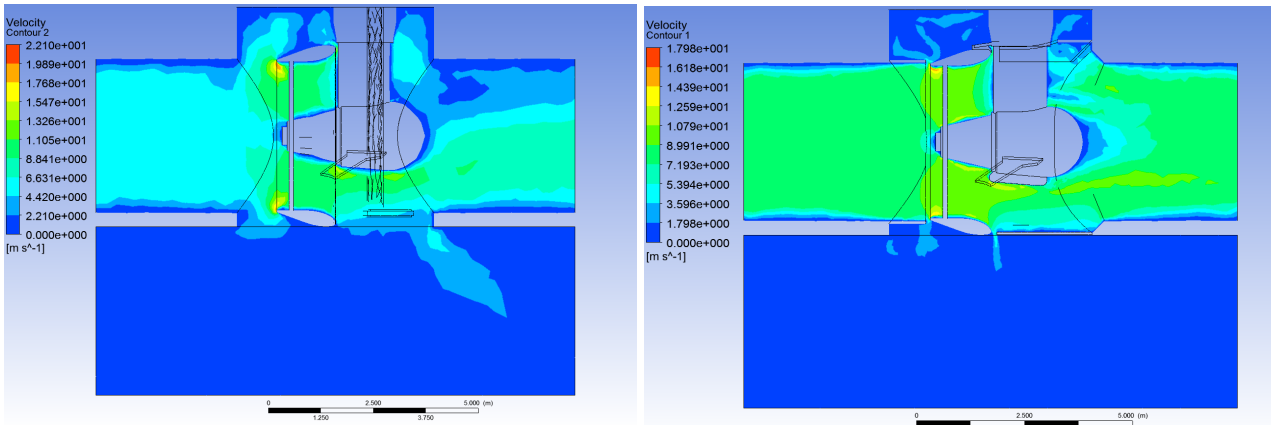

Figure 5. CFD simulation results in the backward direction, velocity field of the flow in the initial design is on the left, simulation of the improved solution's behaviour is on the right. The improvement in that case is about 27 %.

The numerical results are in Table 1 for forward direction and in Table 2 for backward direction and these results are graphically displayed in Fig. 6. As a result of the improvement, the tunnel mode efficiency was increased by 5 % in forward direction and by 27 % in backward direction.

Table 1. Numerical results for forward direction in the tunnel mode.

Design	Initial	Extended	Final
Outlet average mass flow [m^3/s]	89.638	94.512	94.409
Outlet average velocity [m/s]	9.133	9.630	9.619
Tunnel mode efficiency [%]	91	96	96

Table 2. Numerical results for backward direction in the tunnel mode.

Design	Initial	Extended	Final
Outlet average mass flow [m^3/s]	64.586	72.909	81.824
Outlet average velocity [m/s]	6.581	7.429	8.337
Tunnel mode efficiency [%]	66	74	83

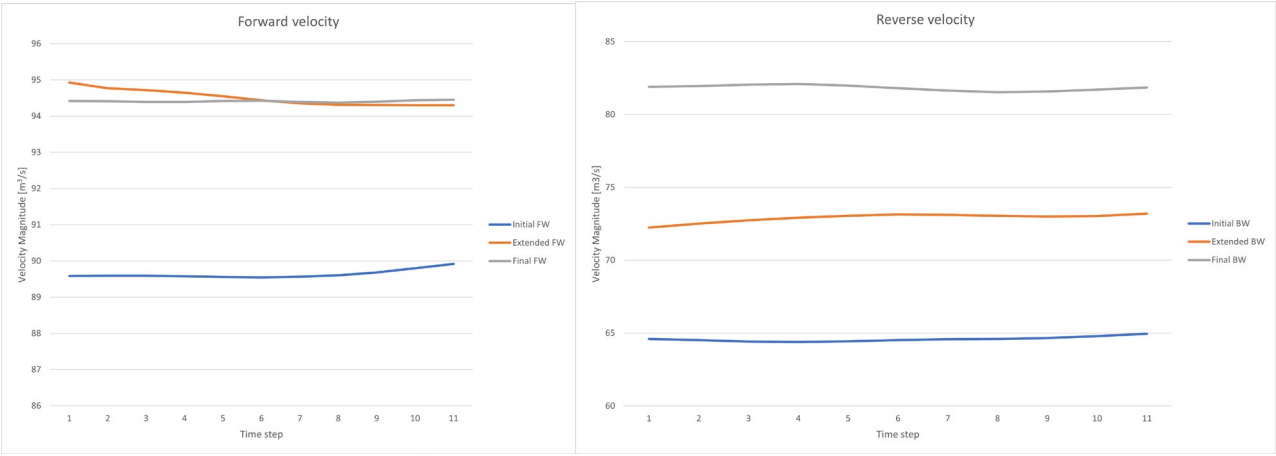

Figure 6. Comparison of efficiency (velocity magnitude) of three thruster design – initial (blue), extended tunnel design without closed bottom well (orange) and final design (grey).

Discussion

Results were promising and there is possibility to improve tunnel flow without expensive equipment or adding large components to the engine room. The main goal was to keep cost as low as possible without adding more equipment. The possibility to add the water jets to control flow of water was also considered, but as seen on tables, the mass flow is dozens of tons per second. That kind of flow needs big water jets and big equipment to supply their energy. When extension was added to tunnel only on the other side of the thruster, flow was improved from 66% to 74% as shown in Table 2. If closing the underside of the well, thrust improved even more, but of course movable flaps are components that needs maintenance and energy to operate. This study demonstrates that with static components flow efficiency can be increased in a cost-efficient way.

References

[1] V. Desai, A. Ayare, B. Mahajan, S. Bade, A Review of Azimuth Thruster, International Journal of Mechanical Engineering 2.10 (2015) 21-24

[2] X.C. Gracia, U.S. Patent US9796462B2. (2015)

[3] S. Brizzolara, E.B. Brizzolara, Long Tunnel Configurations for High Efficiency Thrusters, Fifth International Symposium on Marine Propulsors, Espoo, Finland, June 2017.

[4] I. Funeno, Hydrodynamic Optimal Design of Ducted Azimuth Thrusters, First International Symposium on Marine Propulsors, Trondheim, Norway, 2009.

[5] I. Funeno, Influence of Hydrodynamic Interaction between Ducted Propellers and Struts on Performance of Azimuth Thrusters, Fifth International Symposium on Marine Propulsors, Espoo, Finland, June 2017.

[6] F. Pacuraru, A. Lungu, C. Ungureanu, O. Marcu, Numerical simulation of the flow around a steerable propulsion unit, IOP Conference Series Earth and Environmental Science 12 (2010) 12-32.

[7] N. Bulten, R. Suijkerbuijk, Full scale thruster performance and load determination based on numerical simulations, Third International Symposium on Marine Propulsors, Launceston, Tasmania, Australia, May 2013